Pharmacological inhibition of MCL-1 disrupts mitochondrial cristae and depletes the human neural progenitor cell pool

Marina R. Hanna[1], Madison Yarbrough[2], Melanie Gil[1], James Costanzo[2], and Vivian Gama[1,2,3]

[1]Vanderbilt University, Vanderbilt Brain Institute, Nashville, TN
[2]Vanderbilt University, Cell and Developmental Biology, Nashville, TN.
[3]Vanderbilt University, Vanderbilt Center for Stem Cell Biology, Nashville, TN

[5]Corresponding author

Correspondence should be addressed to:

Vivian Gama
465 21st Avenue South
Vanderbilt University
Nashville, TN 37240-7935
vivian.gama@vanderbilt.edu

Keywords: neural stem cells, MCL-1, mitochondria, cristae, MICOS, OPA1, intermediate progenitors

Abstract

Myeloid Cell Leukemia-1 (MCL-1) is an anti-apoptotic protein that is crucial for early neurodevelopment. Loss of MCL-1 results in embryonic lethal neurodevelopmental defects that cannot be rescued by other anti-apoptotic proteins of the BCL-2 family. Here, we find a non-apoptotic role for MCL-1 in sustaining mitochondrial cristae integrity, fatty acid oxidation (FAO), and neural progenitor identity in human neural stem cells (hNSCs). Pharmacological inhibition of MCL-1 with S63845 disrupts mitochondrial ultrastructure, leading to swollen mitochondria with disorganized cristae and destabilization of the OPA1-MICOS machinery that governs inner membrane architecture. These structural defects are accompanied by impaired lipid droplet accumulation and altered expression of β-oxidation enzymes, revealing a tight link between cristae architecture and metabolic competence. Functionally, in the absence of caspase-mediated cell death, MCL-1 inhibition selectively depletes intermediate progenitor cells and alters neuronal differentiation without affecting proliferation, indicating a direct role in lineage progression. Together, our findings identify MCL-1 as a modulator of cristae organization, linking lipid metabolism to neural progenitor fate. This work establishes mitochondrial inner membrane architecture as an instructive determinant of human neurogenesis and highlights the non-canonical MCL-1 functions as critical regulators of human brain development

Introduction

Neurodevelopment relies on the precise coordination of cellular processes that determine the fate of multipotent *PAX6*-expressing radial glial cells (RGCs)[1–3]. RGCs are the major neural stem cells (NSCs) that give rise to glia and neurons in the human cortex[4,5]. The fate of these NSCs relies on their ability to undergo symmetric or asymmetric division, a process that ultimately determines whether they self-renew or differentiate into specialized cell types[4,5]. NSCs give rise to intermediate progenitor cells (IPCs)[6,7], which are *EOMES (*TBR2*)*-expressing[8,9] cortex-specific transit amplifying cells[10] committed to producing glutamatergic projection neurons of layers two through six[11,12]. Given the high bioenergetic demands and metabolic complexity of NSCs, mitochondrial morphology and function disruption can impair critical stem cell transitions during neurogenesis[13–15]. Despite this, the precise role of mitochondrial morphology and function in these intricate transition states is poorly understood.

Myeloid cell leukemia-1 (MCL-1) is a mitochondrial membrane protein identified as a regulator of mitochondrial morphology through undefined mechanisms that are independent of its canonical anti-apoptotic function[16–20]. Initially only recognized as a member of the B-cell lymphoma 2 (BCL-2) family for its BCL-2 homology-3 (BH3) domain and role in preventing cell death at the outer mitochondrial membrane (OMM)[21], MCL-1 has been well-established to have non-apoptotic functions[17,18,22–26]. Disruption of MCL-1 causes mitochondrial dysfunction in human cardiomyocytes[20,23], as well as improper development of hematopoietic stem cells[27], B cell and T cell progenitors[28], activated B cells[29], and the central nervous system[30]. MCL-1 has been found to also localize at the inner mitochondrial membrane (IMM) where it potentially associates with cristae shaping proteins, such as optic atrophy type 1 (OPA1)[18,19,23]. However, the function of MCL-1 at the IMM is not well understood.

Previous work has reported a close association between MCL-1, mitochondrial morphology, and pluripotent stem cell identity of human embryonic stem cells (hESCs)[17]. Knockdown (KD) of *MCL-1* in hESCs[17] results in an elongated mitochondrial network, a phenotype that has been linked to differentiation[31]. Moreover, *MCL-1*^{KD} hESCs exhibited a loss of key pluripotent transcription factors and identity markers, *OCT4* and *NANOG*[32,33]. Other studies have established a postmitotic period of fate plasticity controlled by mitochondrial morphology during mouse brain development[34,35]. When mitochondrial fusion is disrupted, NSC divide symmetrically, thus expanding the pool of progenitor cells. Conversely, disruption of mitochondrial fragmentation drives NSCs towards premature exit from multipotency, thus inducing lineage differentiation and depletion of the progenitor pool[34,35]. However, the role of MCL-1 in regulating human neurogenesis has not been fully explored.

In vivo mouse studies highlight the importance of MCL-1 in mouse embryonic survival and proper fetal neurodevelopment[26]. A gene swap approach in which the coding sequence of the *Mcl-1* gene in mice was replaced with other anti-apoptotic genes *BCL-2* (*Mcl-1*$^{BCL-2}$), *BCL-XL* (*Mcl-1*$^{Bcl-xL}$), or *A1* (*Mcl-1*^{A1}), resulted in neurodevelopmental defects that could not be rescued by anti-apoptotic functions alone, providing evidence that the noncanonical functions of MCL-1 are indispensable for proper neurodevelopment[26]. Studies in the field have shown that disruption of the FAO pathway promotes asymmetric differentiation of adult mouse NSCs, highlighting FAO's role in regulating stem cell fate decisions[36–39]. Although these studies have established a paradigm for the impact of MCL-1 on FAO and the impact of FAO on mouse adult NSCs, the effects of MCL-1 on the identity of human NSCs remain unknown. Further investigation of the specific non-apoptotic mechanisms of MCL-1 is essential for understanding its role in regulating the mitochondrial processes in human NSCs.

Work from the Opferman and Walensky groups revealed an unexpected link between MCL-1 and fatty acid oxidation (FAO) in cancer cells[22,24,25]. Inhibition of MCL-1 results in decreased oxidation of long-chain fatty acids (LCFAs) in cancer cells[22,24], likely due to the disrupted interaction between MCL-1 and the BH3-like domain of acyl-CoA synthetase long chain family member 1 (ACSL-1). This suggests that MCL-1 is a direct modulator of FAO in cancer cells[25]; however, this has not been investigated in the context of human neurodevelopment.

FAO is a metabolic process critical for energy production and cellular homeostasis that occurs within the mitochondrial matrix and requires LCFAs to pass the OMM and IMM. Starting at the OMM, LCFAs are first activated to acyl-CoA derivatives by ACSL1 and then catalyzed by carnitine palmitoyltransferase I (CPT1) into a fatty acylcarnitine. At the IMM, carnitine palmitoyltransferase II (CPT2) functions to cleave the fatty acylcarnitine and release the fatty acyl-CoA for β-oxidation by Very Long Acyl-CoA Dehydrogenase (VLCAD) at the matrix. The enzymatic breakdown of LCFAs is a multistep process that produces acetyl-CoA, a metabolic byproduct which enters the tricarboxylic acid (TCA) cycle where it generates citrate that *exits* the mitochondria and can be used for histone acetylation[40,41]. Disruption of the FAO pathway promotes asymmetric differentiation of pluripotent and neural stem cells, suggesting a role of FAO in stem cell fate decisions[36–39,42]. Although FAO modulates neurodevelopment and MCL-1 is known to play a role in cancer cell FAO, the role of MCL-1 in FAO during human neurodevelopment has not been explored. Here, we report the non-apoptotic effects of MCL-1 inhibition on mitochondrial and cristae morphology and FAO in NSCs. Our findings provide evidence that MCL-1 maintains the integrity of mitochondrial cristae and neural progenitor cell identity.

Results

MCL-1 inhibition disrupts mitochondrial architecture and inner membrane organization in human neural stem cells

MCL-1 is known for its canonical function as an anti-apoptotic member of the BCL-2 family and is indispensable for the survival of human induced pluripotent stem cells[17], hematopoietic stem cells[27,43], and cardiomyocytes[23]. Similarly, embryonic neural precursor cells depend on MCL-1, as conditional knockout murine models, these cells display widespread apoptosis upon MCL-1 loss[44]. These findings suggest a general dependency on MCL-1 for the survival of neural precursor cells across developmental stages. To examine the effect of MCL-1 inhibition on hNSCs, we differentiated hESCs with SMAD inhibitors, as previously described[45], and treated them with S63845, a selective BH3 mimetic inhibitor of MCL-1, for 24 or 48 hours (**Figure 1A**). Previous studies reported an increase in MCL-1 protein levels upon MCL-1 inhibition, which is speculated to be due to the stabilization of MCL-1 and protection from degradation by proteases when its BH3 domain is occupied[46]. Using RT-qPCR, we observed a downregulation of *MCL-1* at 24 hours of inhibition but not 48 hours (**Supplementary Figure 1A**). Co-treatment with Q-VD-OPh (QVD), a potent pan-caspase inhibitor, did not result in downregulation of *MCL-1* expression (**Supplementary Figure 1B**). As previously reported, we also observed an increase in MCL-1 protein levels in hNSCs at both timepoints (**Supplementary Figures 1C-D**) despite the downregulation of *MCL-1* expression at 24 hours. This increase in MCL-1 protein levels serves as an internal control that the S63845 small molecule inhibitor is effectively inhibiting MCL-1 in hNSCs. However, this upregulation was not observed when hNSCs were co-treated with QVD (**Supplementary Figures 1E-F**).

The mitochondrial network of hNSCs treated with S63845 at both timepoints exhibited a swollen mitochondrial network with greater volume and surface area as revealed by super-resolution

139 microscopy (**Figure 1B**). MCL-1 inhibition at 48 hours resulted in a significant reduction in
140 mitochondrial content, indicating progressive elongation and compaction of the mitochondrial
141 network. The maximum mitochondrial volume and equatorial diameter revealed an expanded
142 mitochondrial network at both timepoints (**Supplementary Figure 2A**). hNSCs co-treated with
143 QVD do not exhibit these mitochondrial network changes (**Supplementary Figure 2B**).
144
145 Due to the critical role of mitochondrial cristae in metabolism regulation, we interrogated whether
146 the effects of MCL-1 inhibition on mitochondrial morphology extended to the ultrastructure of the
147 cristae using transmission electron microscopy (TEM) (**Figure 2A**). The hNSCs treated with MCL-
148 1 inhibitor exhibited an atypical cristae morphology at 48 hours (**Figure 2B**). Three-dimensional
149 FIB-SEM reconstruction further revealed an increase in cristae volume and surface area (**Figures**
150 **2C-D**) but not mitochondrial branching index (MBI) or sphericity (**Supplementary Figure 3A**).
151 MCL-1 inhibition led to extensive loss of cristae organization in S63845-treated cells (**Figure 2A–**
152 **E**). Compared to the densely folded membranes of control mitochondria, those from MCL-1–
153 inhibited cells exhibited swollen matrices and sparse, disordered cristae. Volumetric analyses
154 revealed a sharp increase in both cristae surface area and volume, underscoring the significance
155 of MCL-1 for maintaining inner membrane complexity and structural integrity.
156
157 **MCL-1 activity preserves OPA1 proteostasis and MICOS complex stability**
158 Given the pronounced inner membrane defects, we examined the proteins responsible for cristae
159 shaping and junction formation (**Figure 3A**). The cristae structure is maintained by the
160 mitochondrial contact site and cristae-organizing system (MICOS) complex, composed of the
161 MIC60 subcomplex (MIC60, MIC19, MIC25) and the MIC10 subcomplex (MIC10, MIC26, MIC27)
162 bridged together by MIC13/QIL[47]. The MICOS complex is responsible for establishing junctions
163 that are required for cristae biogenesis in the IMM to increase its surface area for synthesis of
164 adenosine triphosphate (ATP) via oxidative phosphorylation (OXPHOS) through the electron

165 transport chain (ETC)[16,48]. The large GTPase, OPA1, contributes to the stabilization of the MICOS
166 and cristae architecture[49]. The long form of OPA1 (OPA1-L) has a well-established role in IMM
167 fusion[50] and is also critical for the maintenance of cristae lumen width[51]. Cooperatively, the short
168 form of OPA1 (OPA1-S) maintains the length of the cristae lumen[51]. We first examined whether
169 MCL-1 inhibition alone or in combination with QVD alters the expression of *MIC60* or *OPA1* mRNA
170 and found no significant fold change (**Figure 3B-D**). We detected a decrease of OPA1-S1 protein
171 levels at 24 and 48 hours and of OPA1-S2 at 48 hours of MCL-1 plus caspase inhibition, but not
172 with MCL-1 inhibition alone (**Figures 3C-E**). Thus, MCL-1 inhibition disrupts the balance between
173 long (fusion-competent) and short OPA1 isoforms, hindering proteolytic cleavage of OPA1-L into
174 smaller fragments. Immunoblotting analysis for MIC60 and MIC10, the core components of the
175 MICOS subcomplexes, revealed a similar reduction in abundance of MIC10 protein levels at 48
176 hours of MCL-1 inhibition (**Figure 3C**). Co-treatment with the caspase inhibitor QVD did not
177 rescue the levels of MIC10 (**Figure 3E**), indicating that OPA1 processing and MICOS
178 destabilization are not a consequence of caspase activation. We did not observe a change in
179 other MICOS protein levels (**Figure 3C and Supplementary Figure 3B**). These data identify
180 MCL-1 as a critical regulator of mitochondrial inner membrane organization, acting upstream of
181 OPA1- and MICOS-dependent cristae maintenance.
182
183 **MCL-1 inhibition impairs FAO and metabolic coupling.**
184 We predict that the transmembrane FAO enzymes and transport proteins heavily rely on the
185 proper assembly and structure of the OMM and IMM. Previous studies have shown a close
186 interaction between MCL-1 and FAO enzymes in cancer cells[22,25]. A previous study reported a
187 direct interaction with MCL-1 and the BH3-like domain of ACSL1, which is the enzyme responsible
188 for activating fatty acids to fatty acyl CoA in the first step of the FAO pathway (**Figure 4A**). Mouse
189 studies also established the importance of FAO for maintenance of adult NSCs[37,42]. To explore
190 whether the mitochondrial structural perturbations extend to mitochondrial function, we assessed

key regulators of fatty acid β-oxidation. Expression analyses revealed no changes in FAO enzyme transcripts with MCL-1 inhibition alone (**Figure 4B**), but a significant downregulation of *CPT2* transcripts at 24 hours following MCL-1 and caspase inhibition, while *ACSL1* and *CPT1a* levels remained stable (**Figure 4C**). Increased levels of CPT1a were detected at 48 hours following inhibition of MCL-1 (**Figure 4D**). Furthermore, co-treatment with caspase inhibition revealed an increase of CPT1a levels earlier at 24 hours, along with a decrease of CTP2 at 48 hours and VLCAD at both timepoints (**Figure 4E**). The alteration in β-oxidation components persisted despite caspase inhibition, confirming a direct metabolic effect of MCL-1 loss. These findings suggest that MCL-1 supports mitochondrial lipid utilization by sustaining the expression of enzymes critical for fatty acid transport and oxidation.

Fatty acids get stored in lipid droplet organelles when they are not utilized for β-oxidation. Accumulation of lipid droplets upon MCL-1 inhibition was previously reported in cancer cells as a marker of disruption in β-oxidation[25]. To further investigate the impact of MCL-1 on FAO, hNSCs were cultured in nutrient-deficient DMEM media supplemented only with palmitate during treatment with MCL-1 inhibitor, followed by a 2-hour starvation period in HBSS and S63845 (**Figure 5A**). Consistent with impaired β-oxidation, S63845-treated hNSCs accumulated excess neutral lipids when challenged with palmitate as their only resource for fuel (**Figure 5B**). Quantitative imaging revealed increased lipid droplet average and maximum volume (**Figure 5C**), indicative of reduced lipid turnover and a shift toward storage.

MCL-1 maintains neural progenitor identity and supports neuronal differentiation

Given the role of MCL-1 in FAO and the mitochondrial and metabolic perturbations triggered by MCL-1 inhibition, we investigated the effects of MCL-1i treatment on neurogenic progression. Although we did not detect changes in protein levels of hNSC identity markers (**Supplementary Figure 4A**), we observed a significant downregulation of *PAX6* (a marker of neural stem cell

identity) and *EOMES* (the gene encoding TBR2, a marker of intermediate progenitor cells (IPCs)) at 24 hours that was not rescued by QVD co-treatment and persisted into 48 hours with co-treatment (**Supplementary Figure 4B)**. Immunofluorescent imaging revealed a small population of IPCs ($PAX6^-/TBR2^+$) in the culture of hESCs induced with dual SMAD inhibition. IPCs are committed progenitor cells that give rise to glutamatergic projection neurons. MCL-1 inhibition selectively reduced the proportion of $PAX6^-/TBR2^+$ IPCs while sparing $PAX6^+$ radial glia–like progenitors (**Figure 6A**). This loss of IPCs persisted under caspase inhibition (**Figure 6B**), suggesting that MCL-1 is critical for maintaining the identity of this progenitor pool through non-apoptotic mechanisms. To determine how these effects on IPCs impact neuronal differentiation, we first examined the ability of the cells to proliferate using EdU labeling and found no significant changes in late or early S-phase (**Supplementary Figure 5A&B**). To further investigate the potency of neural stem/progenitor cells we examined their ability to differentiate and give rise to newborn neurons using βIII-tubulin staining (**Figure 7**). Control cells formed dense neurite networks with extensive βIII-tubulin labeling, whereas MCL-1–inhibited neurons displayed sparse and truncated processes, reflecting defective neurite extension and maturation (**Figure 7**). When treated with MCL-1 inhibitor, neural stem/progenitor cells gave rise to less newborn neurons with compromised projections that lacked complexity but that was rescued upon co-treatment with QVD. This sheds light on the importance of MCL-1 for the potency of neural stem/progenitor cells to undergo proper differentiation and for newborn neurons to undergo proper maturation (**Figure 7B**). The absence of overt cytotoxicity suggests that MCL-1 directly supports neuronal commitment rather than survival alone.

239 **Discussion**

240 Although MCL-1 has been traditionally studied as an anti-apoptotic BCL-2 family member[21,52],
241 accumulating evidence supports its critical role in maintaining mitochondrial homeostasis across
242 diverse cell types[25,26]. Our findings extend this paradigm to the developing human brain. By
243 combining ultrastructural, molecular, and functional analyses, we report that MCL-1 sustains the
244 integrity of mitochondrial architecture and its functional coupling to metabolic flux. Inhibition of
245 MCL-1 leads to structural collapse of the cristae and disassembly of the MICOS complex as well
246 as OPA1, two scaffolds required for cristae maintenance. Consequently, MCL-1 inhibition impairs
247 FAO metabolism, as evidenced by altered FAO enzyme levels and lipid droplet accumulation. We
248 propose that efficient FAO depends on both cristae surface area and the localization of β-
249 oxidation enzymes to defined subdomains of the inner membrane. These perturbations are
250 accompanied by defects in IPC maintenance and neuronal maturation. Our findings establish a
251 non-apoptotic role for MCL-1 in sustaining mitochondrial organization and metabolic competence,
252 which are indispensable for proper human neurogenesis. Taken together, the data suggest that
253 MCL-1 integrates mitochondrial architecture with metabolic capacity to support progenitor identity.
254

255 While MCL-1 has been reported to influence FAO in cancer cells and to localize to the IMM, its
256 impact on cristae integrity has remained unexplored until now. Our findings bridge this gap by
257 revealing that MCL-1 is indispensable for maintaining cristae organization and metabolic FAO
258 competence in hNSCs. The observed reduction in mitochondrial content upon MCL-1 inhibition
259 likely reflects a compensatory failure where mitochondria are increased in volume and surface
260 but lose metabolic function as apparent by lipid droplet accumulation. We find this disruption to
261 be coupled to a decline in FAO enzymes. Further investigation is required to determine whether
262 ACSL1 localization is affected by MCL inhibition in hNSCs, as reported in cancer cells. Whether
263 ACSL1 integrates into the OMM or needs only to be in close proximity to the OMM for the

activation of LCFAs is not known. Given that the altered FAO enzyme levels were all downstream of ACSL1, this raises the question of whether ACSL1 is a rate-limiting step in the mitochondrial beta-oxidation pathway. If ACSL1 is displaced from the mitochondria, this may disrupt a feedback loop that maintains the expression and stabilization of FAO enzymes, thereby dismantling the FAO signaling pathway and leading to lipid oxidation dysfunction. The alterations in FAO enzyme expression and protein levels accompanied by mitochondrial swelling suggest that MCL-1 coordinates spatial coupling between lipid activation and oxidative metabolism.

Given that efficient FAO is a defining feature of the progenitor metabolic state, this association could represent a key mechanism linking mitochondrial structure and function to the maintenance of stem cell fate. The influence of mitochondrial function on developmental fate decisions is increasingly recognized. *In vivo* and *in vitro* studies have identified a postmitotic window of neurogenic plasticity directed by mitochondrial morphology[44,35,53]. Moreover, disruption of the FAO pathway promotes asymmetric differentiation of adult mouse pluripotent and neural stem cells, signifying a role of FAO in stem cell fate decisions[37,42]. Our data reveal that MCL-1 inhibition disrupts this balance. MCL-1 inhibition does not alter hNSC proliferation, but instead results in reduced intermediate progenitors and impaired neuronal differentiation and maturation. Bioenergetically demanding cells must meet their metabolic needs for proper function and survival. The metabolic intermediates of mitochondrial FAO, such as acetyl-CoA, may alter gene expression via histone modifications (e.g., acetylation) and ultimately influence cell fate decisions. In the delicate process of development, high-energy-demanding cells must maintain a specific metabolic profile for survival, making metabolism a quality-control checkpoint. If a cell does not meet the criteria for differentiation, its fate shifts to maintain tissue integrity.

A key question emerging from this study is whether MCL-1 directly regulates FAO through physical association with lipid import enzymes or indirectly by maintaining cristae topology. We

hypothesize that MCL-1 associates with both MICOS and FAO enzymes at discrete cristae contact points, thereby coupling membrane morphology to metabolic signaling. These results position MCL-1 upstream of the structural regulators OPA1 and MICOS. In alignment with our observations, mutations in cristae-shaping proteins are associated with severe neurodevelopmental disorders, reinforcing the notion that mitochondrial ultrastructure is not only permissive but also instructive in fate specification.

Taken together, our results define a previously unappreciated dimension of MCL-1 function in human neurogenesis, albeit using an *in vitro* experimental paradigm. Beyond its canonical anti-apoptotic role, MCL-1 emerges as a structural and metabolic hub that links cristae architecture, lipid oxidation, and lineage progression. We propose a model in which MCL-1 associates with MICOS and FAO complexes to maintain cristae organization and metabolic flux, thereby sustaining the progenitor state and enabling efficient neuronal differentiation. Future studies dissecting the molecular interfaces between MCL-1, MICOS proteins, and FAO enzymes will be critical for determining whether MCL-1 acts as a scaffold that integrates mitochondrial structure and metabolic signaling. Understanding this connection could illuminate fundamental mechanisms by which mitochondrial morphology encodes developmental potential and may reveal new vulnerabilities in neurodevelopmental and degenerative disorders.

Methods

Human Embryonic Stem Cells (hESCs)

Human embryonic stem cell line, H9 (WA09), was obtained from WiCell Research Institute (Wisconsin). H9s were maintained in mTeSR (STEMCELL Technologies, cat # 85850) media on 6-well plates coated with Matrigel (Corning, cat # 354277) at 37°C with 5% CO2. Culture medium was changed daily. Cells were checked daily for differentiation and were passaged every 3-4 days using Gentle cell dissociation solution (STEMCELL Technologies, cat # 07174). All experiments were performed under the supervision of the Vanderbilt Institutional Human Pluripotent Cell Research Oversight (VIHPCRO) Committee. Cells were periodically checked for contamination.

hESC-derived hNSC culture

H9s were cultured until reaching 70-80% confluency, ensuring minimal differentiation at the colony edges. Cells were dissociated using 1 mL of a Gentle Cell Dissociation Reagent (STEMCELL Technologies, cat # 100-0485) and incubated at 37°C for 8 minutes. 2 mL of DMEM-F12 (Thermo Scientific, cat # 11320033) supplemented with 10 μM of ROCK inhibitor (STEMCELL Technologies, cat # 72307) was added to each well. Cells were gently scraped, pipetted for transfer into a conical tube, and centrifuged at 300 x g for 5 minutes. Cell pellet was resuspended in STEMdiff™ SMADi Neural Induction Medium (NIM) (STEMCELL Technologies, cat # 08581) supplemented with 10 uM ROCK inhibitor. Cell suspension was counted and plated at a density of 2.0-2.5x10^6 cells per well in a 6-well plate. Cells were incubated at 37°C for 7 days, with daily feeding of NIM.

Western blot

Cells were harvested in lysis buffer containing 1% Triton X-100 (Sigma, cat # T9284), 1X complete protease inhibitor cocktail (Roche, cat # 04693159001), 1X PhosSTOP phosphatase inhibitor

333 (Roche, cat # 04906837001), and 0.5mM PMSF (RPI, cat # P20270). Samples were kept on ice
334 and vortexed for 30 seconds every 10 minutes. Lysates were centrifuged at 14,100 x g for 30
335 minutes at 4ºC. Supernatant was collected and protein concentrations were quantified using the
336 Pierce BCA Protein Assay Kit (ThermoScientific, cat # 23225). Western blotting was performed
337 using the Bio-Rad Mini-PROTEAN Electrophoresis System (Bio-Rad, cat # 1658036). Samples
338 were run on 4-20% Mini-PROTEAN TGX gels (Bio-Rad, cat # 4561095). Protein was transferred
339 from gels onto methanol activated PVDF membranes (Bio-Rad, cat # 1620177). All membranes
340 were washed in Tris-buffered saline with 0.1% Tween-20 (TBST) and blocked in TBST containing
341 5% milk for 1 hour at room temperature. Primary antibodies were incubated at listed dilution in
342 TBST containing 5% milk overnight at 4ºC. Secondary antibodies were used at listed dilution in
343 TBST containing 5% milk and incubated for 1 hour at room temperature. Protein signal was
344 developed using either Pierce ECL Western Blot Substrate (32109, ThermoScientific) or
345 SuperSignal West Femto (34094, ThermoScientific), depending on the sensitivity of the primary
346 antibody. Protein signal was visualized using the Amersham Imager 600 (29-0834-61, GE Life
347 Sciences). Acquired images were quantified using Thermo Fisher Scientific iBright Analysis
348 Software and representative images were composed using Affinity Designer 2.
349

Antibody	Source	Catalogue Number	RRID	Dilution	Application
Mouse anti-mitochondria	Abcam	ab92824	AB_10562769	1:200	Immunofluorescence
Mouse anti-PAX6	BD Pharmingen	561462	AB_10715442	1:200	Immunofluorescence
Rabbit anti-EMOES (TBR2)	Cell Signaling Technology	81493	AB_2799974	1:200	Immunofluorescence
Mouse anti-b-Actin	Sigma-Aldrich	A1978	N/A	1:10,000	Western blot
Rabbit anti-cleaved PARP	Cell Signaling Technology	5625S	AB_10699459	1:1000	Western blot
Rabbit anti-MCL-1	Cell Signaling Technology	94296S	AB_2722740	1:1000	Western blot

Rabbit anti-CHCHD3 (MIC19)	Proteintech	25625-1-AP	AB_2687533	1:10,000	Western blot
Rabbit anti-IMMT (MIC60)	Sigma-Aldrich	HPA036164	AB_2674979	1:5000	Western blot
Rabbit anti-OPA-1	Cell Signaling Technology	67589S	AB_2799728	1:5000	Western blot
Rabbit anti-PAX6	Cell Signaling Technology	60433S	AB_2797599	1:500	Western blot
Mouse anti-SOX2	Abcam	ab79351	AB_10710406	1:500	Western blot

RNA extraction and cDNA synthesis

Cells were collected in 1000 µl TRIzol reagent. 200 µl of chloroform was added and the samples were incubated at room temperature for 5 minutes prior to centrifugation at 12,000 x g at 4°C. The aqueous phase was collected and 500 µl of isopropanol was added to precipitate RNA. Samples were incubated for 25 minutes at room temperature, followed by centrifugation at 12,000 x g for 10 minutes at 4°C. The RNA pellet was washed with 75% ethanol, semi-dried, and resuspended in 30 µl of DEPC-treated water. Concentration was measured and 2 µg per sample was treated with DNAse (New England Biolabs #M0303) prior to generating cDNA using the manufacturer's protocol (Thermo Fisher #4368814).

Quantitative PCR (RT-qPCR)

50 ng of cDNA sample was used to run RT-qPCR using 20 µM of the primers listed in the table. QuantStudio 3 Real-Time PCR machine, SYBR green master mix (Thermo Fisher #4364346), and manufacturer instructions were used to set up the assay.

Target	Forward Primer	Reverse Primer
GAPDH	ACAACTTTGGTATCGTGGAAGG	GCCATCACGCCACAGTTTC
GPI	GTGTACCTTCTAGTCCCGCC	GGTCAAGCTGAAGTGGTTGAAGC
MCL-1	GTGCCTTTGTGGCTAAACACT	AGTCCCGTTTTGTCCTTACGA

MIC19	GAGGCGGACGAGAATGAGAAC	ACCAGAATACCGCTGAGACTTC
MIC60	CGATTCAGTCGGGTCCACTAA	AGCTGGAGTATCTCCCTTTTGT
OPA1	TGTGAGGTCTGCCAGTCTTTA	TGTCCTTAATTGGGGTCGTTG
PAX6	TGGGCAGGTATTACGAGACTG	ACTCCCGCTTATACTGGGCTA
SOX2	CCATGCAGGTTGACACCGTTG	TCGGCAGACTGATTCAAATAATACAG
TBR2	GTGCCCACGTCTACCTGTG	CCTGCCCTGTTTCGTAATGAT

Immunofluorescence

Cells were plated on 35 mm glass-bottom dishes (glass thickness of 0.16-0.19 mm) for confocal spinning disk immunofluorescence. Cells were fixed with 4% paraformaldehyde for 20 min and permeabilized in 1% Triton-X-100 for 10 min at room temperature. After blocking in 10% BSA for 1 hour, cells were treated with primary and secondary antibodies using standard methods. Primary antibodies were incubated at listed dilution in 10% BSA overnight at 4ºC. Secondary antibodies were used at listed dilution in 10% BSA and incubated for 1 hour at room temperature. The nuclear stain used was HOECHST (Thermo Scientific, cat # H3570) and cells were mounted in Fluoromount-G (Electron Microscopy Sciences #17984-25) prior to imaging. Cells were labeled for EdU using the manufacturer's protocol (Thermo Fisher #C10340). Lipid droplet staining was done live using BODIPY (Cayman Chemical Company #25892). Calls were incubated at 37ºC for 15 minutes in 4 μM BODIPY prior to fixation in 4% PFA.

Spinning Disk Confocal image acquisition

Images were acquired using a Nikon Spinning Disk Confocal outfitted with a Yokogawa CSU-X1 spinning disk head, Andor DU-897 EMCCD camera, and high-speed piezo [z] stage. All 100X images were acquired with a step size of 0.2 μm, while 20X images were acquired with a step size of 2 μm. Image processing and quantification was performed using NIS Elements (Nikon) and all representative images were generated using Fiji.

385 For mitochondrial morphology, we segmented mitochondria in 3D and performed skeletonization
386 of the resulting 3D mask. Skeleton major axis length, volume, and surface area measurements
387 were exported into GraphPad Prism v9.
388

389 **Tissue Preparation for TEM and FIB-SEM**

390 Neural progenitor cells were plated at $1.5x10^6$ cells per 35 mm dish on Matrigel. The cells were
391 washed with 1X PBS (3X), fixed in 2.5% glutaraldehyde in 0.1 M cacodylate prewarmed to 37ºC,
392 left to cool down at room temperature for 1hr, and placed at 4ºC for an additional 24-48 hour of
393 fixation. Cells were washed from fixative with 1X PBS (3x). Samples were sequentially post-fixed
394 using the OTO method: 1.5% potassium ferrocyanide, 1% OsO4 in 0.1 M cacodylate for 30
395 minutes on ice, then 1% thiocarbohydrazide for 10 minutes, followed by 1% OsO4 in ddH2O for
396 10 minutes. Samples are then enblock stained with 2% uranyl acetate followed by lead aspartate.
397 The samples were then dehydrated in a graded ethanol series and infiltrated with Durcupan resin
398 using acetone as the transition solvent. The resin was polymerized at 60ºC for 48 hours. For TEM,
399 sections were cut on a Leica UC7 at a nominal thickness of 50 nm with no post-section staining.
400 For FIB-SEM, samples were prepared as previously described[54].
401

402 **TEM image acquisition and Cristae Scoring**

403 Sections were imaged with either a ThermoFisher Scientific Tecnai T12 operating at 100 keV
404 using an AMT nanosprint5 CMOS camera or a JEOL 2100+ operating at 200 keV using an AMT
405 nanosprint15 II CMOS camera. In both cases, AMT acquisition software was used for imaging.
406 The TEM images were analyzed using cristae scoring (Lam et. Al, 2021)[55]. The files were first
407 renamed to blind the scoring process. The images were then blindly scored. A score was provided
408 for each mitochondrion based on the quality of the cristae. The scoring rubric was as follows: 0 -
409 there were no crista, 1 - more than 50% of the mitochondrial area did not have cristae, 2 - more

410 than 25% of the mitochondria was without cristae, 3 - lots of cristae but irregular in structure, and
411 4 - many cristae that are regular structures.
412
413 **FIB-SEM image acquisition**
414 Sections were imaged with Zeiss Crossbeam 550 FIB-SEM using ATLAS5 software for
415 automated volumetric acquisition. Sample blocked were polished with a diamond knife and coated
416 with platinum. Platinum pads were deposited via GIS on ROIs of interest, followed by milling in
417 tracking marks and coating with GIS carbon. Milling was performed using a 700 pA Ga beam at
418 8 nm slice depth, imaging was performed 1.5 keV electron beam using the in column ESB detector
419 for imaging at 8 nm pixels to make isotropic voxels. Volumetric slice alignments were performed
420 in ATLAS5 using the two-window alignment method.
421
422 **FIB-SEM mitochondrial image analysis**
423 FIB-SEM stacks were first cropped using Fiji is just Image J (FIJI). In the FIB-SEM stacks, none
424 of the cells imaged were able to be visualized completely. Therefore, the crop size and location
425 were selected by choosing a cell with bright, visible mitochondria. The crop was 500 x 500 pixels
426 with a 3,000 nm depth. The cropped image was then imported into the FIJI LabKit plugin for
427 segmentation[56]. For segmentation, each mitochondrion was manually traced with a separate label
428 ID. Quality control was then performed following each mitochondrion through the entirety of the
429 Z-stack and tracking all locations where the membranes connect. Any mitochondria that merged
430 in any of the frames were labeled with the same label ID. The cropped FIB-SEM image and the
431 proofread segmentation masks were imported into the IMARIS software. Ortho slices in the XY
432 and XZ planes were added, and the proofread mask was selected to be identified by ID. This
433 identifies each separate mitochondrion. Any mitochondria that were still split were manually
434 combined in the IMARIS software using the unify feature. A clipping plane was then added.
435 Animations were made using the animations tab in IMARIS with 50 frames per second and 1,000

436 frames total. Still images were captured using the screenshot feature. Volume quantification was
437 done by volume measurement provided in the statistics tab in IMARIS. Surface area quantification
438 was manually calculating using volume and sphericity measurements from the IMARIS statistics
439 tab using the equation: $\frac{\pi^{\frac{1}{3}}(6*Volume)^{\frac{2}{3}}}{Sphericity}$. Lastly, the mitochondrial branching index (MBI), was
440 calculated by obtaining the BoundingBox00 length A (longest side) and BoundingBox00 length C
441 (Shortest side) in the Vantage 2D tab and then dividing Length C/ Length A manually[57].
442
443 **FIB-SEM cristae image analysis**
444 The same FIB-SEM cropped images were used for the segmentation of the cristae. The cropped
445 images were imported into FIJI and applied Contrast Limited Adaptive Histogram Equalization
446 (CLAHE) to increase contrast. They were then imported into the LabKit plugin for segmentation.
447 Each crista was manually traced, and all the cristae within one mitochondrion were labeled with
448 the same label ID. Quality control was then performed, ensuring each mitochondrion had all its
449 cristae labeled with the same ID. The cropped FIB-SEM image and the proofread segmentation
450 masks were imported into the IMARIS software. Ortho slices in the XY and XZ planes were added,
451 and the proofread mask was selected by ID. This identifies each separate mitochondrion's cristae.
452 Any errors in the cristae mask were merged using the unify feature in IMARIS. A clipping plane
453 was then added to show the mitochondria throughout the entire z-plane. Animations were made
454 using the animations tab in IMARIS with 50 frames per second and with 1,000 frames total. Still
455 images were taken using the snapshot feature. Volume quantification was done by volume
456 measurement provided in the statistics tab in IMARIS. Surface Area quantification was manually
457 calculated using volume and sphericity measurements from IMARIS statistics tab using the
458 equation: $\frac{\pi^{\frac{1}{3}}(6*Volume)^{\frac{2}{3}}}{Sphericity}$. Cristae measurements were then normalized to the corresponding
459 mitochondria by dividing the crista measurement by the mitochondrion measurement (i.e.,

460 $\frac{Crista\ Volume}{Mitochonrion\ Volume}$. The mitochondria segmentation was then added to the same IMARIS file as a
461 second surface. The label was chosen by ID, and the surface type was changed to transparent
462 to show the cristae within those mitochondria. Images were taken using the snapshot function,
463 and animations were made with 50 frames per second and 1,000 frames total.
464

465 **Statistical analysis**

466 All experiments were performed with at least 3 biological replicates. Statistical significance was
467 determined by one-way, repeated measures one-way ANOVA, or t-test as appropriate for each
468 experiment. Significance was assessed using Fisher's protected least significance difference test.
469 GraphPad Prism v9 was used for all statistical analysis and data visualization. Error bars in all
470 bar graphs represent the standard error of the mean unless otherwise noted in the figure. No
471 outliers were removed from the analyses. For all statistical analyses, a significant difference was
472 accepted when $P < 0.05$.

473

474
475
476
477

478 **Figure Legends**

479 **Figure 1. S63845 impacts mitochondrial content and morphology.**

480 (A) Schematic detailing the neural induction of human embryonic stem cells (hESCs) using SMAD
481 inhibition (SMADi) for the derivation of the human neural stem cells (hNSCs) tissue culture model.
482 hNSCs are maintained in neural induction media (NIM) with daily media changes until they are
483 passaged on day 7. hNSCs are given a 24-hour acclimation period on day 8 before treatment on
484 day 9 with 1μm S63845 (MCL-1 inhibitor), and DMSO as the control group. Samples were then
485 collected at 24- and 48-hours post-treatment on days 10 and 11 after which cells were fixed and
486 stained for imaging on a SoRa spinning disk confocal (SDC) microscope. (B) Immunofluorescent
487 images of mitochondria (anti-mito in magenta) and nuclei (Hoechst in cyan) acquired on SoRA
488 SDC at 100X (scale bar = 40μm). Representative images (n=3) of 24- and 48-hours post-
489 treatment with DMSO control and S63845 (MCL-1 inhibitor). Quantification of mitochondrial
490 content and average measures of mitochondrial morphology. Nine images were acquired per
491 condition and plotted in gray. Each large, open-shape data point represents the mean per
492 biological replicate. Shape of data point corresponds to each biological replicate (open circle for
493 n=1, open square for n=2, and open triangle for n=3). Means of the biological replicates were
494 analyzed using a parametric two-tailed unpaired t-test with a Welch's Correction. Error bars
495 represent standard error of the mean.

496

497 **Figure 2. MCL-1 inhibition compromises mitochondrial cristae integrity.**

498 (A) Schematic detailing the neural induction of human embryonic stem cells (hESCs) using SMAD
499 inhibition (SMADi) for the derivation of the human neural stem cells (hNSCs) tissue culture model.
500 hNSCs are maintained in neural induction media (NIM) with daily media changes until they are
501 passaged on day 7. hNSCs are given a 24-hour acclimation period on day 8 before treatment on
502 day 9 with 1μm MCL-1 inhibitor (S63845 MCL-1i) with DMSO as the control group. Samples were
503 then collected at 48-hours post-treatment on day 11 after which cells were fixed and processed

504 for transmission electron microscopy (TEM) or focused ion beam-scanning electron microscopy
505 (FIB-SEM). (B) Representative TEM images (n=3) of hNSC mitochondrial cristae 48-hours post-
506 treatment with DMSO control and S63845 MCL-1 inhibitor. Scale bar = 600nm. (C) 3-dimensional
507 reconstructions of mitochondria and cristae after 48-hour treatment with S63845 (MCL1 inhibitor)
508 (scale bar = 0.5μm). (D) Quantification of cristae changes from 3-dimensional reconstruction.
509 Each cristae volume and surface area was normalized to (divided by) the corresponding
510 mitochondrion volume and surface area, respectively, and multiplied by 100 to get the percentage
511 of change. Each data point shown is an individual mitochondrion. Data were analyzed using a
512 parametric two-tailed unpaired t-test with a Welch's correction. (E) Volumetric still frames of
513 mitochondrial cristae 3-D reconstruction of NSCs at 48 hours post-treatment with DMSO control
514 and S63845 (MCL-1 inhibitor) segmented from FIB-SEM volume images. Scale bar = 3000 nm.
515
516 **Figure 3. S63845 and QVD co-treatment reveal altered levels of cristae-shaping proteins.**
517 (A) Schematic detailing the neural induction of human embryonic stem cells (hESCs) using
518 SMADi. hNSCs are maintained in neural induction media (NIM) with daily media changes until
519 they are passaged on day 7. hNSCs are given a 24-hour acclimation period on day 8 before
520 treatment on day 9 with 1μm S63845 (MCL-1 inhibitor), plus or minus 25 μM QVD co-treatment,
521 with DMSO or DMSO+QVD as the control groups. Samples were then collected at 24- and 48-
522 hours post-treatment on days 10 and 11, respectively. Cells were collected in either Trizol for real-
523 time quantitative polymerase chain reaction (RT-qPCR) or protease inhibitor-containing lysis
524 buffer for western blot. (B) Quantified relative expression of *OPA1* and *MIC60* after 24- and 48-
525 hour treatments with DMSO control and S63845 (MCL-1 inhibitor). (C) Left panel: representative
526 images (n=3) of OPA1-L, OPA1-S1, OPA1-S2, MIC60, and MIC10 after 24- and 48-hours of
527 treatment with DMSO control and S63845 (MCL-1 inhibitor). Right panel: quantified band density.
528 (D) Quantified relative expression of *OPA1* and *MIC60* after 24- and 48-hour S63845 plus QVD
529 co-treatment. (E) Representative images (n=3) and quantified band density of OPA1-L, OPA1-

530 S1, OPA1-S2, MIC60, and MIC10 after 24- and 48- hour S63845 plus QVD co-treatment. Each
531 data point represents a biological replicate. Shape of data point corresponds to each biological
532 replicate (circle for n=1, square for n=2, and triangle for n=3). Data analyzed using a parametric
533 two-tailed unpaired t-test with a Welch's Correction. Error bars represent standard error of the
534 mean.
535
536 **Figure 4. S63845 and QVD co-treatment results in downregulation of carnitine**
537 **palmitoyltransferase and altered levels of FAO enzymes.**
538 (A) Schematic of the mitochondrial fatty acid beta-oxidation pathway (B) Quantified relative
539 expression of FAO enzymes after 24- and 48-hours post-treatment with DMSO and S63845
540 (MCL-1 inhibitor). (C) Quantified relative expression of FAO enzymes after 24- and 48-hour
541 S63845 plus QVD co-treatment. (D) Representative images (n=3) and quantified band density of
542 ACSL1, CPT1a, CPT2, and VLCAD after 24- and 48-hours of treatment with DMSO control and
543 S63845 (MCL-1 inhibitor). (E) Representative images (n=3) and quantified band density of
544 ACSL1, CPT1a, CPT2, and VLCAD after 24- and 48- hour S63845 plus QVD co-treatment. Each
545 data point on the graph represents a biological replicate. Shape of data point corresponds to each
546 biological replicate (circle for n=1, square for n=2, and triangle for n=3). Data analyzed using a
547 parametric two-tailed unpaired t-test with Welch's Correction. Error bars represent standard error
548 of the mean.
549
550 **Figure 5. hNSCs supplemented with palmitate and treated with S63845 accumulate lipid**
551 **droplets.**
552 (A) Schematic of experimental design. On day 9 post-induction, hNSCs were treated with S63845
553 in nutrient deficient DMEM media (-glucose, -glutamine, -pyruvate) and supplemented with
554 100μM of palmitate for 12 hours followed by a 2-hour starvation in HBSS. Cells were then live
555 stained with BODIPY and Hoechst prior to PFA fixation. (B) Representative fluorescent images

556 (n=3) of lipid droplets (BODIPY in magenta) and nuclei (Hoechst in cyan) were acquired on a
557 spinning disk confocal microscope at 100X (scale bar = 40μm). (C) Quantification of lipid droplet
558 content, average volume, and maximum volume. Six images were acquired per condition and
559 plotted in gray with shape corresponding to each biological replicate. Each open-shape data point
560 represents the mean per biological replicate. Shape of data point corresponds to each biological
561 replicate (open circle for n=1, open square for n=2, and open triangle for n=3). Means of the
562 biological replicates were analyzed using a parametric two-tailed unpaired t-test with a Welch's
563 Correction. Error bars represent standard error of the mean.
564
565 **Figure 6. S63845 results in depletion of TBR2^{+}/PAX6^{-} IPCs independent of cell death.**
566 Representative fluorescent images (n=3) of nuclear identity markers TBR2 (green), PAX6
567 (magenta), and nuclei (Hoechst in blue) were acquired on a spinning disk confocal microscope at
568 20X (scale bar = 200μm). Intermediate progenitor cells (IPCs) identified by presence of TBR2 and
569 absence of PAX6. (A) Quantified percentage of IPCs after 24- and 48-hour treatments with
570 S63845 (MCL-1 inhibitor). (B) Quantified percentage of IPCs after 24- and 48-hour S63845 plus
571 QVD co-treatment. Quantification of IPCs manually counted and normalized to total cell count for
572 final percentage output. Seven images were acquired per condition and plotted in gray. Each
573 large, open-shape data point represents the mean per biological replicate. Shape of data point
574 corresponds to biological replicate (open circle for n=1, open square for n=2, and open triangle
575 for n=3). Mean of biological replicates analyzed using a two-tailed paired parametric t-test.
576
577 **Figure 7. S63845 results in depletion of BIII-Tubulin^{+} newborn neurons.**
578 (A) Representative fluorescent images of each biological replicate (n=3) of hNSCs treated with
579 S63845 alone or with QVD co-treatment. Newborn neurons labeled with BIII-Tubulin (white) and
580 nuclei (Hoechst in blue) were imaged on a spinning disk confocal microscope at 60X (scale bar =
581 100μm).
582

583 **Acknowledgements**

584 We thank Caleb Hayes, Caroline Bodnya, Meeros Khattaie, Dr. Antentor J. Hinton, Dr. Zer Vue,
585 and Dr. Oleg Kovtun for their technical advice and assistance. This work was supported by 2R35
586 GM128915-01NIGMS (VG), Training Program in Stem Cell and Regenerative Developmental
587 Biology 5T32HD007502-25 (MRH). 2R25GM134979-06 (MY), and HHMI Gilliam Fellowship
588 GT15720 (MG). All TEM and FIB-SEM imaging and image analysis were performed in part using
589 the Vanderbilt Cell Imaging Shared Resource, which is supported by NIH grants 1S10OD012324-
590 01 and 1S10OD021630-01. The authors declare no competing financial interests.

591 **Author contributions**

592 M. R. Hanna and V. Gama conceived the study, designed experiments, interpreted data, and
593 wrote the manuscript. V. Gama supervised the research. M. R. Hanna designed, conducted, and
594 analyzed all cell biology experiments, with technical assistance from M. Gil, M. Yarbrough, and J.
595 Costanzo. E. Krystofiak performed TEM and FIB-SEM tissue preparation and imaging. M.
596 Yarbrough performed 3D reconstruction and analysis of FIB-SEM data. All authors edited the
597 document.

598

References

1. Hansen, D. V., Lui, J. H., Parker, P. R. L. & Kriegstein, A. R. Neurogenic radial glia in the outer subventricular zone of human neocortex. *Nature* **464**, 554–561 (2010).
2. Pollen, A. A., Nowakowski, T. J., Chen, J., Retallack, H., Sandoval-Espinosa, C., Nicholas, C. R., Shuga, J., Liu, S. J., Oldham, M. C., Diaz, A., Lim, D. A., Leyrat, A. A., West, J. A. & Kriegstein, A. R. Molecular Identity of Human Outer Radial Glia during Cortical Development. *Cell* **163**, 55–67 (2015).
3. Beattie, R. & Hippenmeyer, S. Mechanisms of radial glia progenitor cell lineage progression. *FEBS Lett* **591**, 3993–4008 (2017).
4. Silbereis, J. C., Pochareddy, S., Zhu, Y., Li, M. & Sestan, N. The Cellular and Molecular Landscapes of the Developing Human Central Nervous System. *Neuron* **89**, 248–268 (2016).
5. Molnár, Z., Clowry, G. J., Šestan, N., Alzu'bi, A., Bakken, T., Hevner, R. F., Hüppi, P. S., Kostović, I., Rakic, P., Anton, E. S., Edwards, D., Garcez, P., Hoerder-Suabedissen, A. & Kriegstein, A. New insights into the development of the human cerebral cortex. *J Anat* **235**, 432–451 (2019).
6. Haubensak, W., Attardo, A., Denk, W. & Huttner, W. B. Neurons arise in the basal neuroepithelium of the early mammalian telencephalon: A major site of neurogenesis. *Proceedings of the National Academy of Sciences* **101**, 3196–3201 (2004).
7. Yoon, K.-J., Koo, B.-K., Im, S.-K., Jeong, H.-W., Ghim, J., Kwon, M., Moon, J.-S., Miyata, T. & Kong, Y.-Y. Mind Bomb 1-Expressing Intermediate Progenitors Generate Notch Signaling to Maintain Radial Glial Cells. *Neuron* **58**, 519–531 (2008).
8. Englund, C., Fink, A., Lau, C., Pham, D., Daza, R. A. M., Bulfone, A., Kowalczyk, T. & Hevner, R. F. Pax6, Tbr2, and Tbr1 Are Expressed Sequentially by Radial Glia, Intermediate Progenitor Cells, and Postmitotic Neurons in Developing Neocortex. *J. Neurosci.* **25**, 247–251 (2005).
9. Kawaguchi, A., Ikawa, T., Kasukawa, T., Ueda, H. R., Kurimoto, K., Saitou, M. & Matsuzaki, F. Single-cell gene profiling defines differential progenitor subclasses in mammalian neurogenesis. *Development* **135**, 3113–3124 (2008).
10. Tajbakhsh, S. Stem cell: what's in a name? *Nat Rep Stem Cells* 1–1 (2009) doi:10.1038/stemcells.2009.90.
11. Kowalczyk, T., Pontious, A., Englund, C., Daza, R. A. M., Bedogni, F., Hodge, R., Attardo, A., Bell, C., Huttner, W. B. & Hevner, R. F. Intermediate Neuronal Progenitors (Basal Progenitors) Produce Pyramidal–Projection Neurons for All Layers of Cerebral Cortex. *Cerebral Cortex* **19**, 2439–2450 (2009).
12. Hevner, R. F. Intermediate progenitors and Tbr2 in cortical development. *Journal of Anatomy* **235**, 616–625 (2019).
13. Copp, A. J. & Greene, N. D. E. Neural tube defects—disorders of neurulation and related embryonic processes. *WIREs Developmental Biology* **2**, 213–227 (2013).
14. Baum, T. & Gama, V. Dynamic properties of mitochondria during human corticogenesis. *Development* **148**, dev194183 (2021).
15. Robertson, G. L., Riffle, S., Patel, M., Bodnya, C., Marshall, A., Beasley, H. K., Garza-Lopez, E., Shao, J., Vue, Z., Hinton, A., Jr, Stoll, M. S., de Wet, S., Theart, R. P., Chakrabarty, R. P., Loos, B., Chandel, N. S., Mears, J. A. & Gama, V. DRP1 mutations associated with EMPF1 encephalopathy alter mitochondrial membrane potential and metabolic programs. *Journal of Cell Science* **136**, jcs260370 (2023).
16. Colina-Tenorio, L., Horten, P., Pfanner, N. & Rampelt, H. Shaping the mitochondrial inner membrane in health and disease. *Journal of Internal Medicine* **287**, 645–664 (2020).
17. Rasmussen, M. L., Kline, L. A., Park, K. P., Ortolano, N. A., Romero-Morales, A. I., Anthony, C. C., Beckermann, K. E. & Gama, V. A Non-apoptotic Function of MCL-1 in Promoting

Pluripotency and Modulating Mitochondrial Dynamics in Stem Cells. *Stem Cell Reports* **10**, 684–692 (2018).

18. Perciavalle, R. M., Stewart, D. P., Koss, B., Lynch, J., Milasta, S., Bathina, M., Temirov, J., Cleland, M. M., Pelletier, S., Schuetz, J. D., Youle, R. J., Green, D. R. & Opferman, J. T. Anti-apoptotic MCL-1 localizes to the mitochondrial matrix and couples mitochondrial fusion to respiration. *Nature Cell Biology* **14**, 575–583 (2012).
19. Perciavalle, R. M. & Opferman, J. T. Delving deeper: MCL-1's contributions to normal and cancer biology. *Trends in Cell Biology* **23**, 22–29 (2013).
20. Wang, X., Bathina, M., Lynch, J., Koss, B., Calabrese, C., Frase, S., Schuetz, J. D., Rehg, J. E. & Opferman, J. T. Deletion of MCL-1 causes lethal cardiac failure and mitochondrial dysfunction. *Genes Dev* **27**, 1351–1364 (2013).
21. Kozopas, K. M., Yang, T., Buchan, H. L., Zhou, P. & Craig, R. W. MCLI, a gene expressed in programmed myeloid cell differentiation, has sequence similarity to BCL2. *Proc. Natl. Acad. Sci. USA* 5 (1993).
22. Escudero, S., Zaganjor, E., Lee, S., Mill, C. P., Morgan, A. M., Crawford, E. B., Chen, J., Wales, T. E., Mourtada, R., Luccarelli, J., Bird, G. H., Steidl, U., Engen, J. R., Haigis, M. C., Opferman, J. T. & Walensky, L. D. Dynamic Regulation of Long-Chain Fatty Acid Oxidation by a Noncanonical Interaction between the MCL-1 BH3 Helix and VLCAD. *Molecular Cell* **69**, 729-743.e7 (2018).
23. Rasmussen, M. L., Taneja, N., Neininger, A. C., Wang, L., Robertson, G. L., Riffle, S. N., Shi, L., Knollmann, B. C., Burnette, D. T. & Gama, V. MCL-1 Inhibition by Selective BH3 Mimetics Disrupts Mitochondrial Dynamics Causing Loss of Viability and Functionality of Human Cardiomyocytes. *iScience* **23**, (2020).
24. Prew, M. S., Adhikary, U., Choi, D. W., Portero, E. P., Paulo, J. A., Gowda, P., Budhraja, A., Opferman, J. T., Gygi, S. P., Danial, N. N. & Walensky, L. D. MCL-1 is a master regulator of cancer dependency on fatty acid oxidation. *Cell Reports* **41**, 111445 (2022).
25. Wright, T., Turnis, M. E., Grace, C. R., Li, X., Brakefield, L. A., Wang, Y.-D., Xu, H., Kaminska, E., Climer, L. K., Mukiza, T. O., Chang, C.-L., Moldoveanu, T. & Opferman, J. T. Anti-apoptotic MCL-1 promotes long-chain fatty acid oxidation through interaction with ACSL1. *Molecular Cell* **0**, (2024).
26. Brinkmann, K., McArthur, K., Malelang, S., Gibson, L., Tee, A., Elahee Doomun, S. N., Rowe, C. L., Arandjelovic, P., Marchingo, J. M., D'Silva, D., Bachem, A., Monard, S., Whelan, L. G., Dewson, G., Putoczki, T. L., Bouillet, P., Fu, N. Y., Brown, K. K., Kueh, A. J., Wimmer, V. C., Herold, M. J., Thomas, T., Voss, A. K. & Strasser, A. Relative importance of the anti-apoptotic versus apoptosis-unrelated functions of MCL-1 in vivo. *Science* **389**, 1003–1011 (2025).
27. Opferman, J. T., Iwasaki, H., Ong, C. C., Suh, H., Mizuno, S., Akashi, K. & Korsmeyer, S. J. Obligate role of anti-apoptotic MCL-1 in the survival of hematopoietic stem cells. *Science* **307**, 1101–1104 (2005).
28. Opferman, J. T., Letai, A., Beard, C., Sorcinelli, M. D., Ong, C. C. & Korsmeyer, S. J. Development and maintenance of B and T lymphocytes requires antiapoptotic MCL-1. *Nature* **426**, 671–676 (2003).
29. Vikstrom, I., Carotta, S., Lüthje, K., Peperzak, V., Jost, P. J., Glaser, S., Busslinger, M., Bouillet, P., Strasser, A., Nutt, S. L. & Tarlinton, D. M. Mcl-1 is essential for germinal center formation and B cell memory. *Science* **330**, 1095–1099 (2010).
30. Arbour, N., Vanderluit, J. L., Le Grand, J. N., Jahani-Asl, A., Ruzhynsky, V. A., Cheung, E. C. C., Kelly, M. A., MacKenzie, A. E., Park, D. S., Opferman, J. T. & Slack, R. S. Mcl-1 Is a Key Regulator of Apoptosis during CNS Development and after DNA Damage. *Journal of Neuroscience* **28**, 6068–6078 (2008).
31. Iwata, R., Casimir, P. & Vanderhaeghen, P. Mitochondrial dynamics in postmitotic cells regulate neurogenesis. *Science* **369**, 858–862 (2020).

32. Takahashi, K. & Yamanaka, S. Induction of Pluripotent Stem Cells from Mouse Embryonic and Adult Fibroblast Cultures by Defined Factors. *Cell* **126**, 663–676 (2006).
33. Takahashi, K., Tanabe, K., Ohnuki, M., Narita, M., Ichisaka, T., Tomoda, K. & Yamanaka, S. Induction of Pluripotent Stem Cells from Adult Human Fibroblasts by Defined Factors. *Cell* **131**, 861–872 (2007).
34. Khacho, M., Clark, A., Svoboda, D. S., Azzi, J., MacLaurin, J. G., Meghaizel, C., Sesaki, H., Lagace, D. C., Germain, M., Harper, M.-E., Park, D. S. & Slack, R. S. Mitochondrial Dynamics Impacts Stem Cell Identity and Fate Decisions by Regulating a Nuclear Transcriptional Program. *Cell Stem Cell* **19**, 232–247 (2016).
35. Iwata Ryohei, Casimir Pierre, & Vanderhaeghen Pierre. Mitochondrial dynamics in postmitotic cells regulate neurogenesis. *Science* **369**, 858–862 (2020).
36. Xie, Z., Jones, A., Deeney, J. T., Hur, S. K. & Bankaitis, V. A. Inborn Errors of Long-Chain Fatty Acid β-Oxidation Link Neural Stem Cell Self-Renewal to Autism. *Cell Rep* **14**, 991–999 (2016).
37. Knobloch, M., Pilz, G.-A., Ghesquière, B., Kovacs, W. J., Wegleiter, T., Moore, D. L., Hruzova, M., Zamboni, N., Carmeliet, P. & Jessberger, S. A Fatty Acid Oxidation-Dependent Metabolic Shift Regulates Adult Neural Stem Cell Activity. *Cell Reports* **20**, 2144–2155 (2017).
38. Stoll, E. A., Makin, R., Sweet, I. R., Trevelyan, A. J., Miwa, S., Horner, P. J. & Turnbull, D. M. Neural Stem Cells in the Adult Subventricular Zone Oxidize Fatty Acids to Produce Energy and Support Neurogenic Activity. *Stem Cells* **33**, 2306–2319 (2015).
39. Khoa, L. T. P., Tsan, Y.-C., Mao, F., Kremer, D. M., Sajjakulnukit, P., Zhang, L., Zhou, B., Tong, X., Bhanu, N. V., Choudhary, C., Garcia, B. A., Yin, L., Smith, G. D., Saunders, T. L., Bielas, S. L., Lyssiotis, C. A. & Dou, Y. Histone Acetyltransferase MOF Blocks Acquisition of Quiescence in Ground-State ESCs through Activating Fatty Acid Oxidation. *Cell Stem Cell* **27**, 441-458.e10 (2020).
40. Schvartzman, J. M., Thompson, C. B. & Finley, L. W. S. Metabolic regulation of chromatin modifications and gene expression. *J Cell Biol* **217**, 2247–2259 (2018).
41. Arnold, P. K., Jackson, B. T., Paras, K. I., Brunner, J. S., Hart, M. L., Newsom, O. J., Alibeckoff, S. P., Endress, J., Drill, E., Sullivan, L. B. & Finley, L. W. S. A non-canonical tricarboxylic acid cycle underlies cellular identity. *Nature* **603**, 477–481 (2022).
42. Ramosaj, M., Madsen, S., Maillard, V., Scandella, V., Sudria-Lopez, D., Yuizumi, N., Telley, L. & Knobloch, M. Lipid droplet availability affects neural stem/progenitor cell metabolism and proliferation. *Nat Commun* **12**, 7362 (2021).
43. Opferman, J. T. & Kothari, A. Anti-apoptotic BCL-2 family members in development. *Cell Death Differ* **25**, 37–45 (2018).
44. Khacho, M. & Slack, R. S. Mitochondrial dynamics in the regulation of neurogenesis: From development to the adult brain. *Developmental Dynamics* **247**, 47–53 (2018).
45. Chambers, S. M., Fasano, C. A., Papapetrou, E. P., Tomishima, M., Sadelain, M. & Studer, L. Highly efficient neural conversion of human ES and iPS cells by dual inhibition of SMAD signaling. *Nat Biotechnol* **27**, 275–280 (2009).
46. Tantawy, S. I., Timofeeva, N., Hernandez, A., Sarkar, A. & Gandhi, V. Decoding the mechanism behind MCL-1 inhibitors: A pathway to understanding MCL-1 protein stability. *Oncotarget* **14**, 653–655 (2023).
47. Eramo, M. J., Lisnyak, V., Formosa, L. E. & Ryan, M. T. The 'mitochondrial contact site and cristae organising system' (MICOS) in health and human disease. *J Biochem* **167**, 243–255 (2020).
48. Stephan, T., Brüser, C., Deckers, M., Steyer, A. M., Balzarotti, F., Barbot, M., Behr, T. S., Heim, G., Hübner, W., Ilgen, P., Lange, F., Pacheu-Grau, D., Pape, J. K., Stoldt, S., Huser, T., Hell, S. W., Möbius, W., Rehling, P., Riedel, D. & Jakobs, S. MICOS assembly controls mitochondrial inner membrane remodeling and crista junction redistribution to mediate cristae formation. *EMBO J* **39**, e104105 (2020).

49. Glytsou, C., Calvo, E., Cogliati, S., Mehrotra, A., Anastasia, I., Rigoni, G., Raimondi, A., Shintani, N., Loureiro, M., Vazquez, J., Pellegrini, L., Enriquez, J. A., Scorrano, L. & Soriano, M. E. Optic Atrophy 1 Is Epistatic to the Core MICOS Component MIC60 in Mitochondrial Cristae Shape Control. *Cell Reports* **17**, 3024–3034 (2016).
50. Hu, C., Shu, L., Huang, X., Yu, J., Li, L., Gong, L., Yang, M., Wu, Z., Gao, Z., Zhao, Y., Chen, L. & Song, Z. OPA1 and MICOS Regulate mitochondrial crista dynamics and formation. *Cell Death Dis* **11**, 1–17 (2020).
51. von der Malsburg, A., Sapp, G. M., Zuccaro, K. E., von Appen, A., Moss, F. R., Kalia, R., Bennett, J. A., Abriata, L. A., Dal Peraro, M., van der Laan, M., Frost, A. & Aydin, H. Structural mechanism of mitochondrial membrane remodelling by human OPA1. *Nature* **620**, 1101–1108 (2023).
52. Green, D. R. & Llambi, F. Cell Death Signaling. *Cold Spring Harb Perspect Biol* **7**, a006080 (2015).
53. Iwata, R., Casimir, P., Erkol, E., Boubakar, L., Planque, M., Gallego López, I. M., Ditkowska, M., Gaspariunaite, V., Beckers, S., Remans, D., Vints, K., Vandekeere, A., Poovathingal, S., Bird, M., Vlaeminck, I., Creemers, E., Wierda, K., Corthout, N., Vermeersch, P., Carpentier, S., Davie, K., Mazzone, M., Gounko, N. V., Aerts, S., Ghesquière, B., Fendt, S.-M. & Vanderhaeghen, P. Mitochondria metabolism sets the species-specific tempo of neuronal development. *Science* **379**, eabn4705 (2023).
54. Boassa, D., Deerinck, T. J., Bushong, E. A., Thor, A. & Ellisman, M. Preparation of Cultured Cells for Serial Block Face Scanning Electron Microscopy (SBEM). https://www.protocols.io/view/preparation-of-cultured-cells-for-serial-block-fac-b5naq5ae (2022).
55. Lam, J., Katti, P., Biete, M., Mungai, M., AshShareef, S., Neikirk, K., Garza Lopez, E., Vue, Z., Christensen, T. A., Beasley, H. K., Rodman, T. A., Murray, S. A., Salisbury, J. L., Glancy, B., Shao, J., Pereira, R. O., Abel, E. D. & Hinton, A. A Universal Approach to Analyzing Transmission Electron Microscopy with ImageJ. *Cells* **10**, 2177 (2021).
56. Arzt, M., Deschamps, J., Schmied, C., Pietzsch, T., Schmidt, D., Tomancak, P., Haase, R. & Jug, F. LABKIT: Labeling and Segmentation Toolkit for Big Image Data. *Front. Comput. Sci.* **4**, (2022).
57. Vue, Z., Garza-Lopez, E., Neikirk, K., Katti, P., Vang, L., Beasley, H., Shao, J., Marshall, A. G., Crabtree, A., Murphy, A. C., Jenkins, B. C., Prasad, P., Evans, C., Taylor, B., Mungai, M., Killion, M., Stephens, D., Christensen, T. A., Lam, J., Rodriguez, B., Phillips, M. A., Daneshgar, N., Koh, H., Koh, A., Davis, J., Devine, N., Saleem, M., Scudese, E., Arnold, K. R., Vanessa Chavarin, V., Daniel Robinson, R., Chakraborty, M., Gaddy, J. A., Sweetwyne, M. T., Wilson, G., Zaganjor, E., Kezos, J., Dondi, C., Reddy, A. K., Glancy, B., Kirabo, A., Quintana, A. M., Dai, D., Ocorr, K., Murray, S. A., Damo, S. M., Exil, V., Riggs, B., Mobley, B. C., Gomez, J. A., McReynolds, M. R. & Hinton, A. 3D reconstruction of murine mitochondria reveals changes in structure during aging linked to the MICOS complex. *Aging Cell* **22**, e14009 (2023).

Figure 1

A

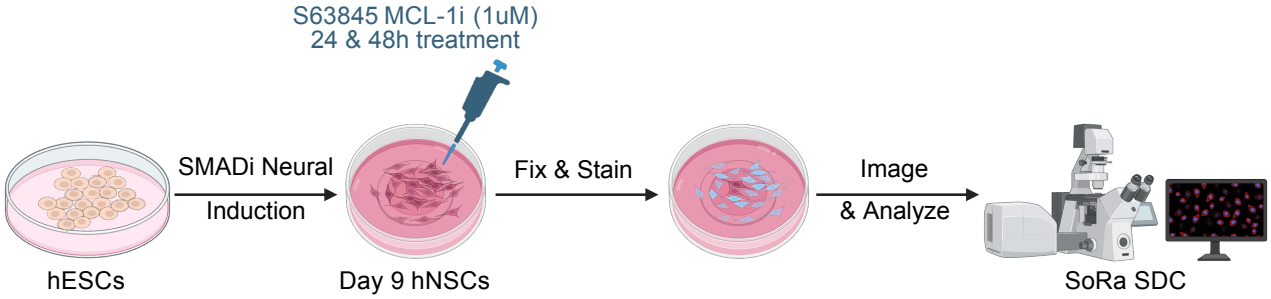
S63845 MCL-1i (1uM)
24 & 48h treatment
SMADi Neural
Induction
Fix & Stain
Image
& Analyze
hESCs
Day 9 hNSCs
SoRa SDC

B

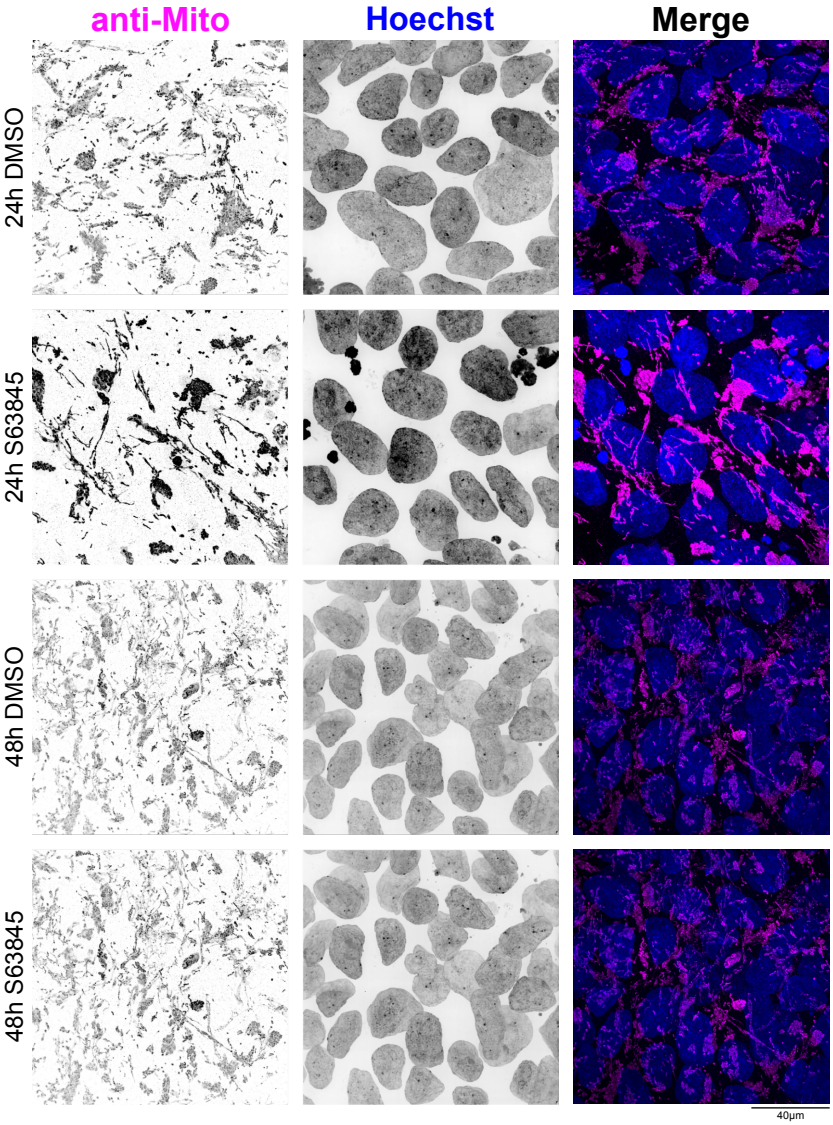
anti-Mito
Hoechst
Merge
24h DMSO
24h S63845
48h DMSO
48h S63845
40µm

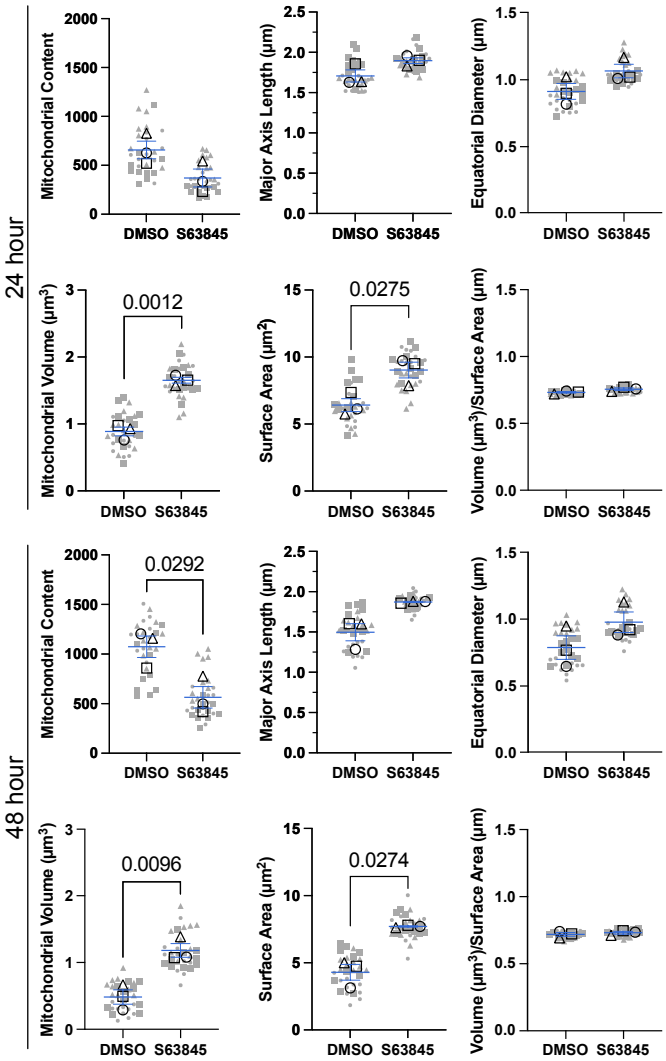
24 hour
48 hour
Mitochondrial Content
Major Axis Length (µm)
Equatorial Diameter (µm)
Mitochondrial Volume (µm³)
Surface Area (µm²)
Volume (µm³)/Surface Area (µm)
DMSO
S63845
0.0012
0.0275
0.0292
0.0096
0.0274

Figure 2

A

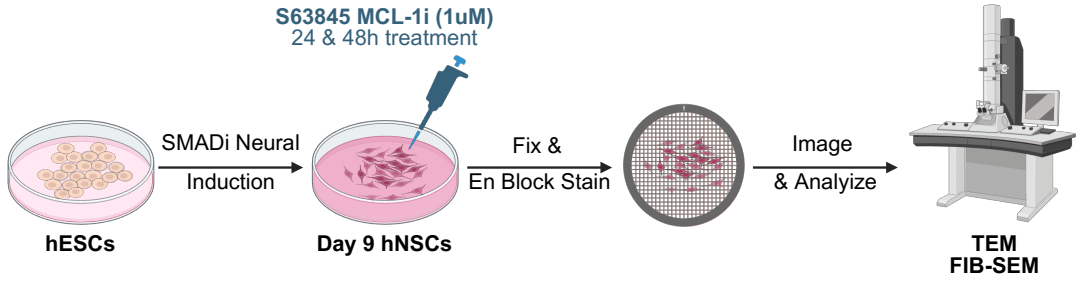

B

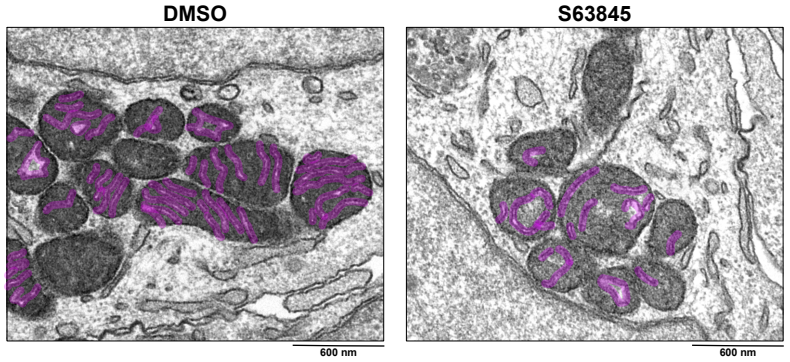

C

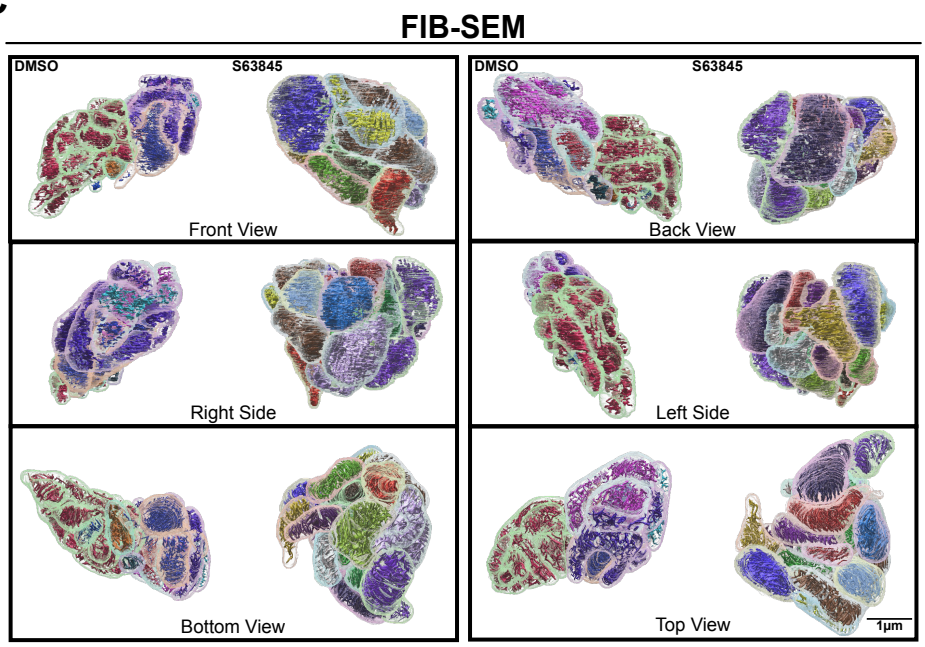

D

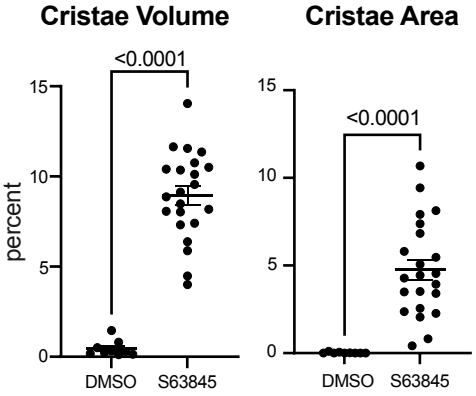

E

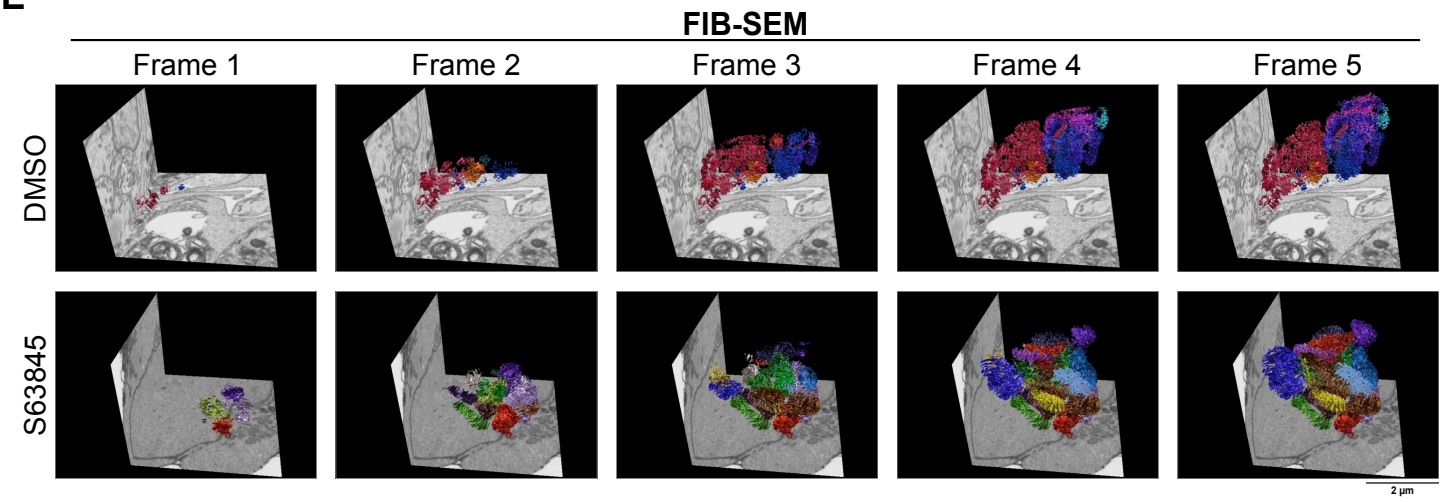

Figure 3

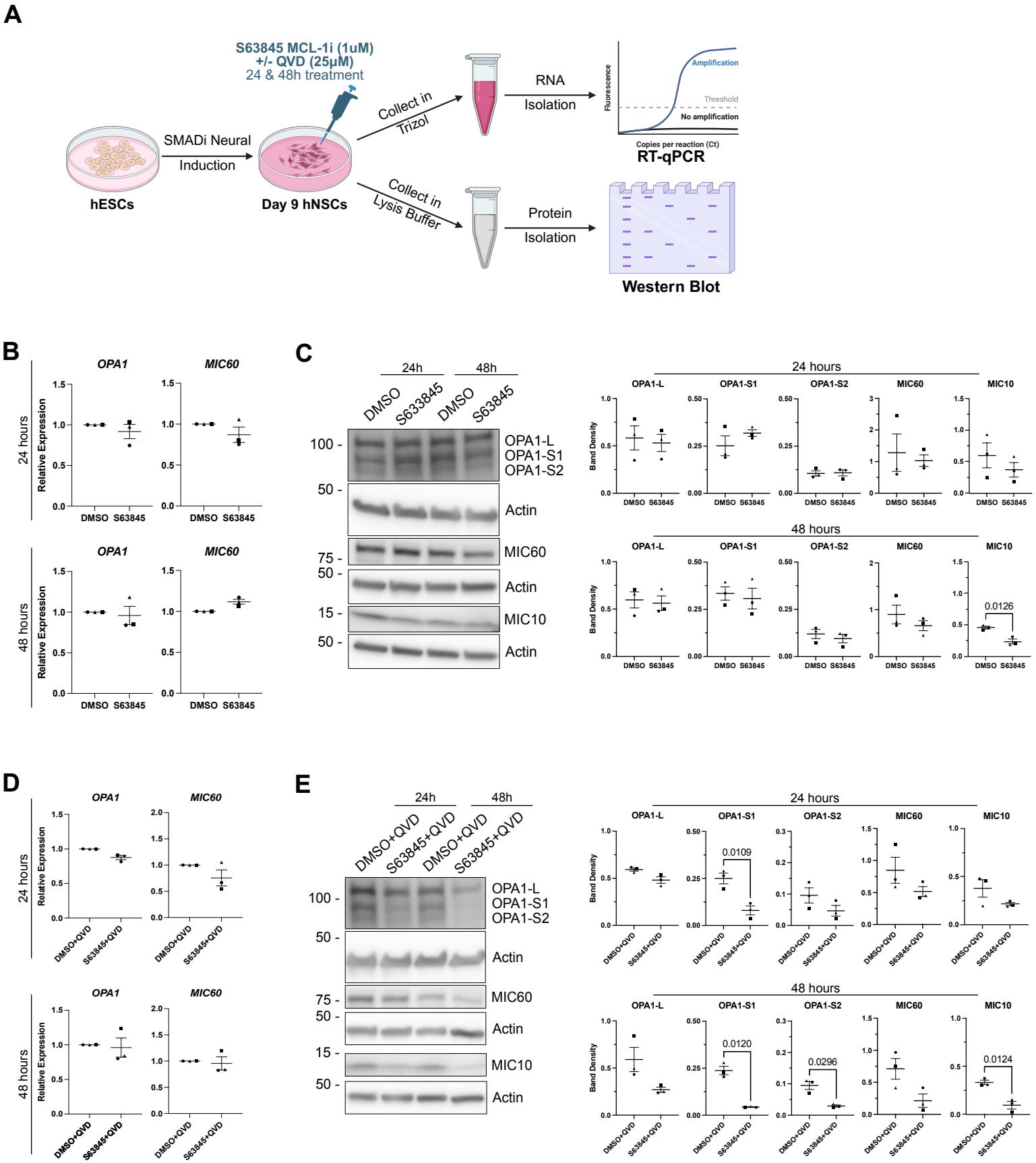
A
S63845 MCL-1i (1uM)
+/- QVD (25μM)
24 & 48h treatment
SMADi Neural
Induction
hESCs
Day 9 hNSCs
Collect in
Trizol
Collect in
Lysis Buffer
RNA
Isolation
Protein
Isolation
Amplification
Threshold
No amplification
Fluorescence
Copies per reaction (Ct)
RT-qPCR
Western Blot
B
OPA1
MIC60
24 hours
48 hours
Relative Expression
DMSO
S63845
C
24h
48h
DMSO
S633845
S63845
OPA1-L
OPA1-S1
OPA1-S2
Actin
MIC60
MIC10
Band Density
0.0126
D
DMSO+QVD
S63845+QVD
E
0.0109
0.0120
0.0296
0.0124

Figure 4

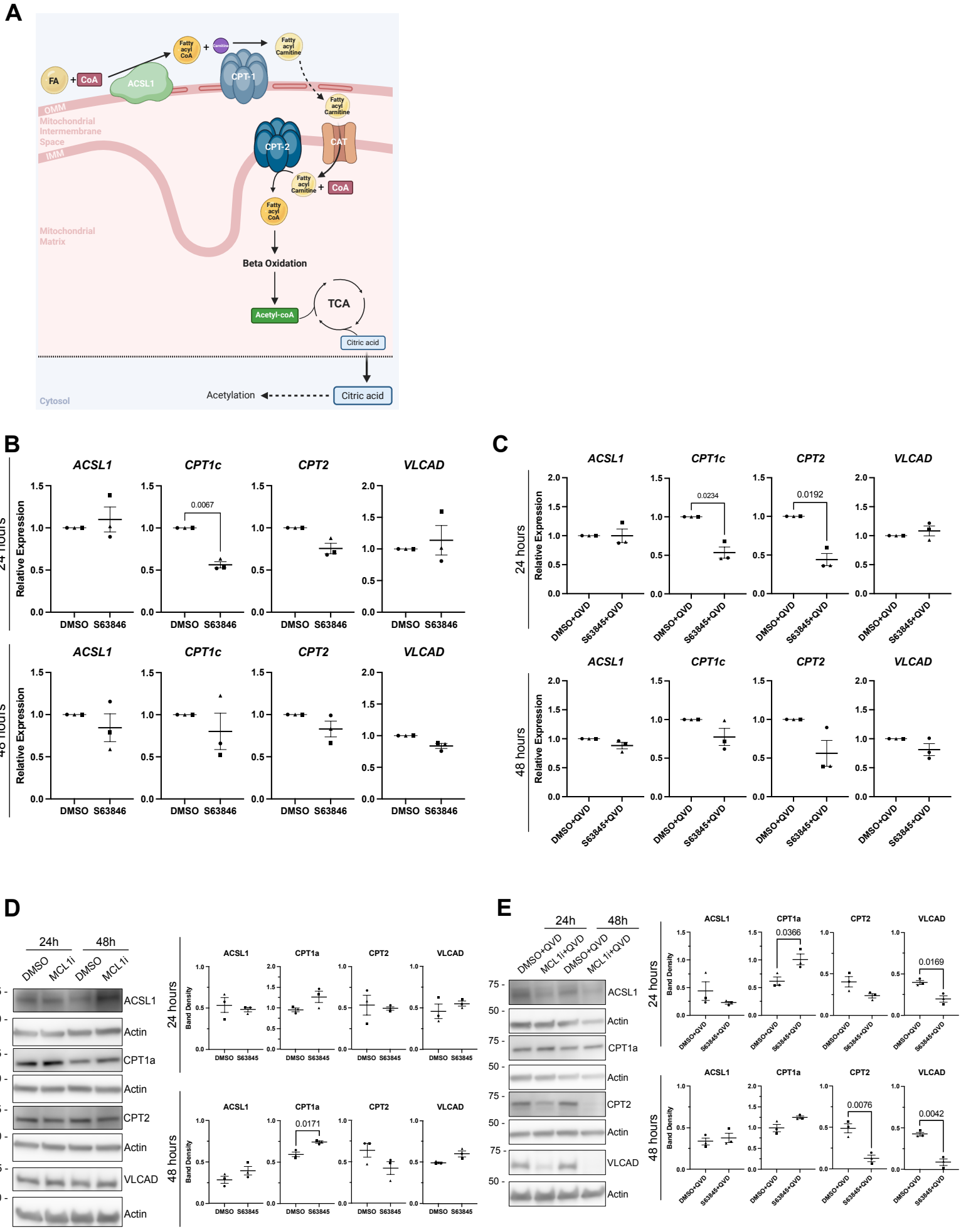
A
FA
CoA
ACSL1
Fatty acyl CoA
Carnitine
CPT-1
Fatty acyl Carnitine
OMM
Mitochondrial Intermembrane Space
IMM
CPT-2
CAT
Fatty acyl Carnitine
CoA
Fatty acyl CoA
Mitochondrial Matrix
Beta Oxidation
Acetyl-coA
TCA
Citric acid
Cytosol
Acetylation
Citric acid
B
24 hours
48 hours
Relative Expression
ACSL1
CPT1c
CPT2
VLCAD
0.0067
DMSO
S63846
C
0.0234
0.0192
DMSO+QVD
S63845+QVD
D
24h
48h
DMSO
MCL1i
ACSL1
Actin
CPT1a
CPT2
VLCAD
Band Density
CPT1a
0.0171
S63845
E
DMSO+QVD
MCL1i+QVD
0.0366
0.0169
0.0076
0.0042

Figure 5

A

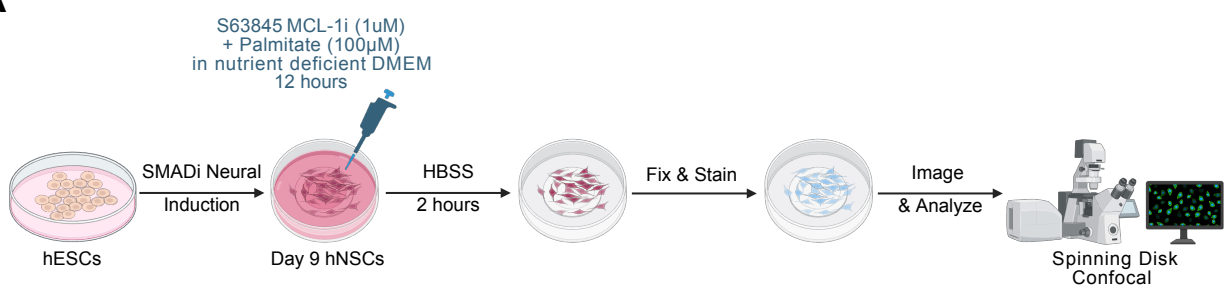
S63845 MCL-1i (1uM)
+ Palmitate (100μM)
in nutrient deficient DMEM
12 hours
SMADi Neural
Induction
HBSS
2 hours
Fix & Stain
Image
& Analyze
hESCs
Day 9 hNSCs
Spinning Disk
Confocal

B

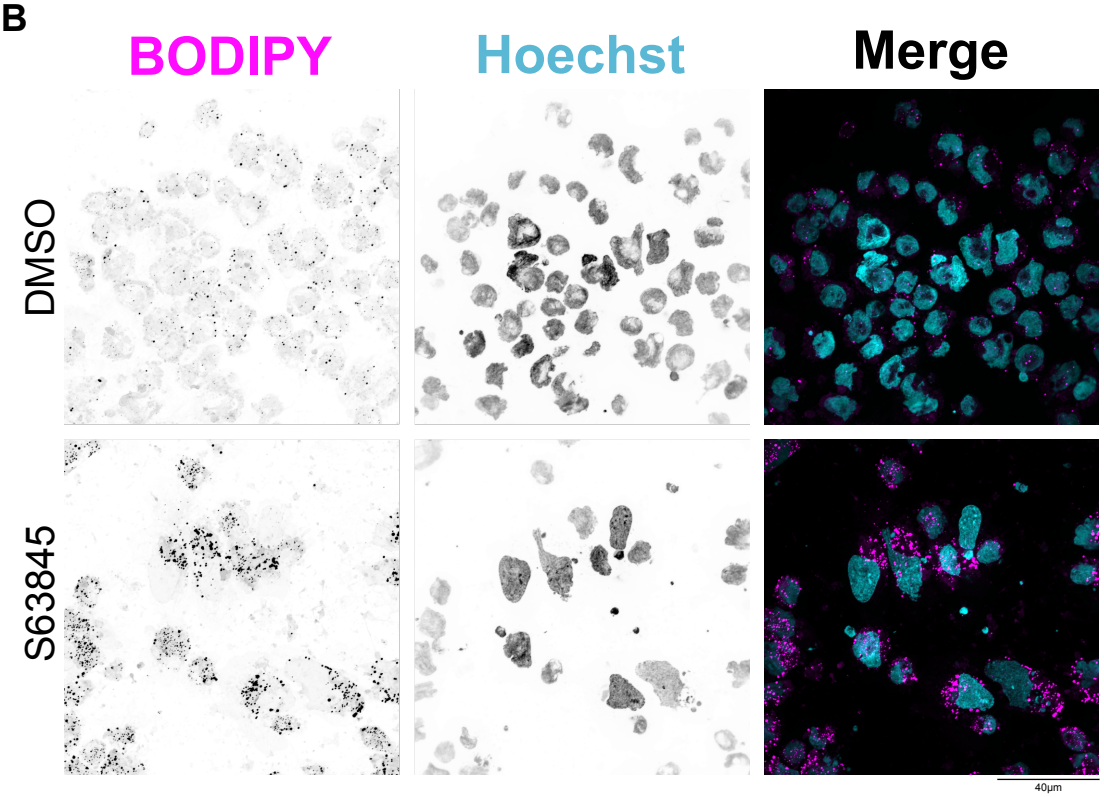
BODIPY
Hoechst
Merge
DMSO
S63845
40μm

C

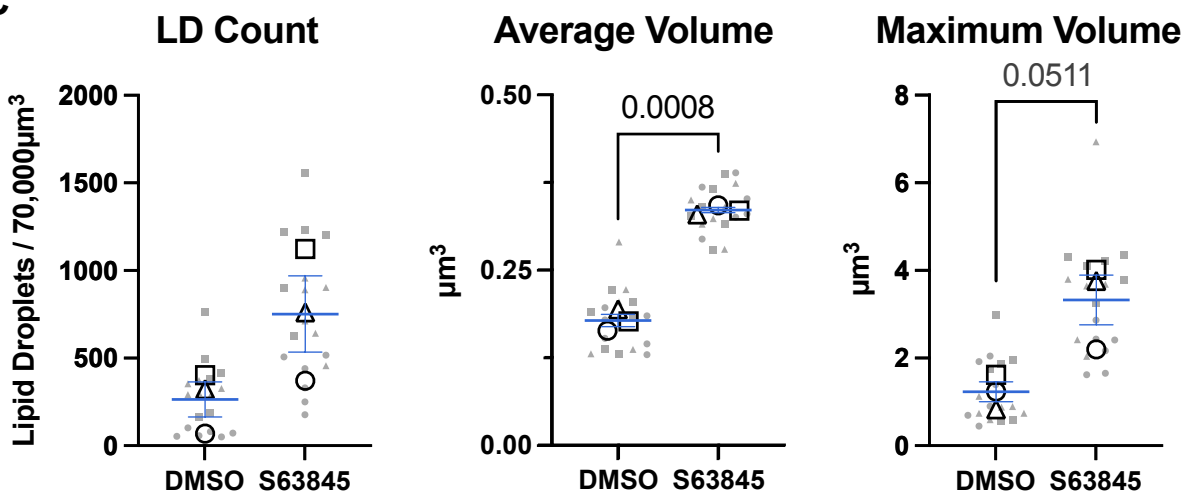
LD Count
Average Volume
Maximum Volume
Lipid Droplets / 70,000μm³
2000
1500
1000
500
0
DMSO
S63845
0.50
0.25
0.00
μm³
0.0008
8
6
4
2
0
0.0511

Figure 6

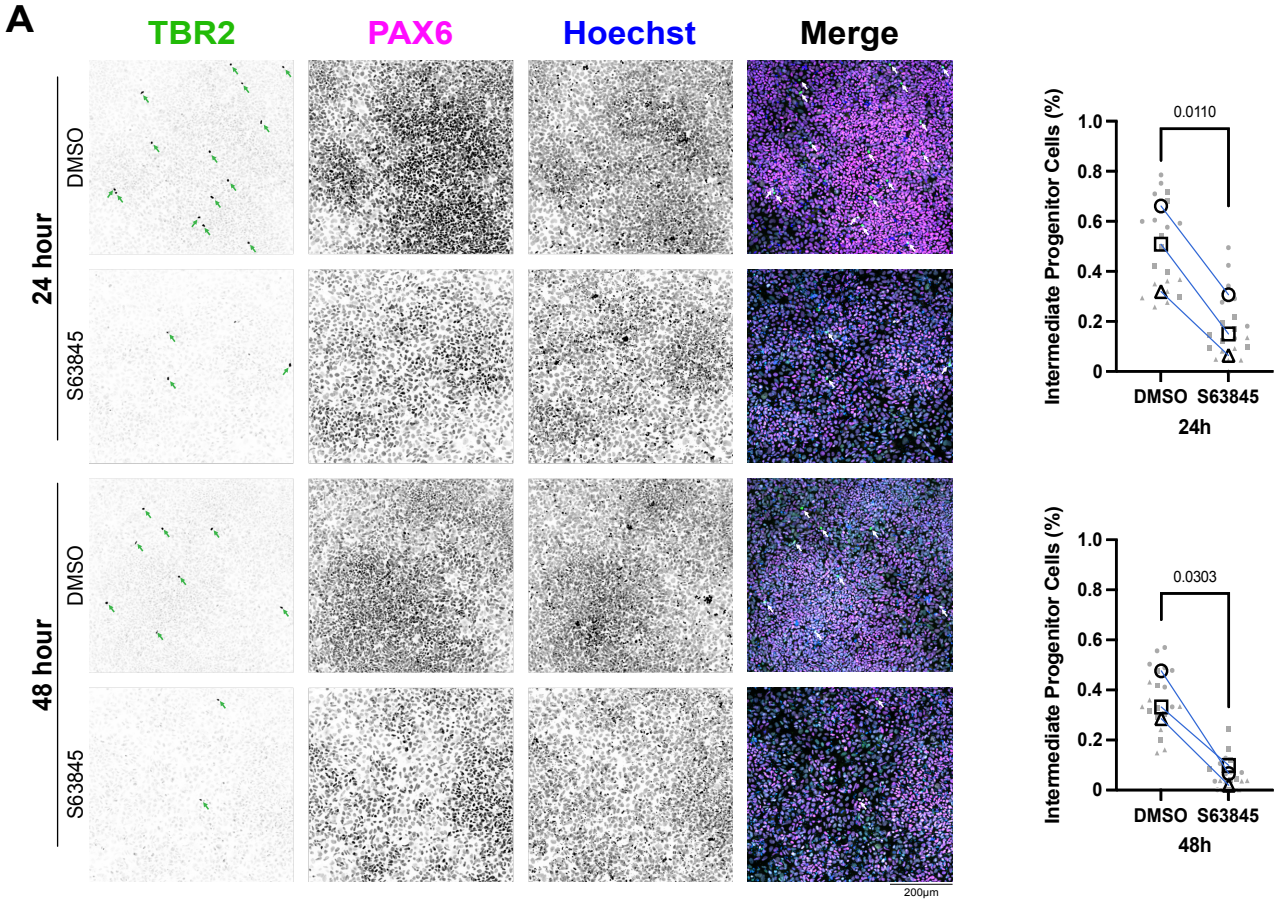
A
TBR2
PAX6
Hoechst
Merge
24 hour
DMSO
S63845
48 hour
DMSO
S63845
200µm
Intermediate Progenitor Cells (%)
0.0110
DMSO
S63845
24h
0.0303
48h

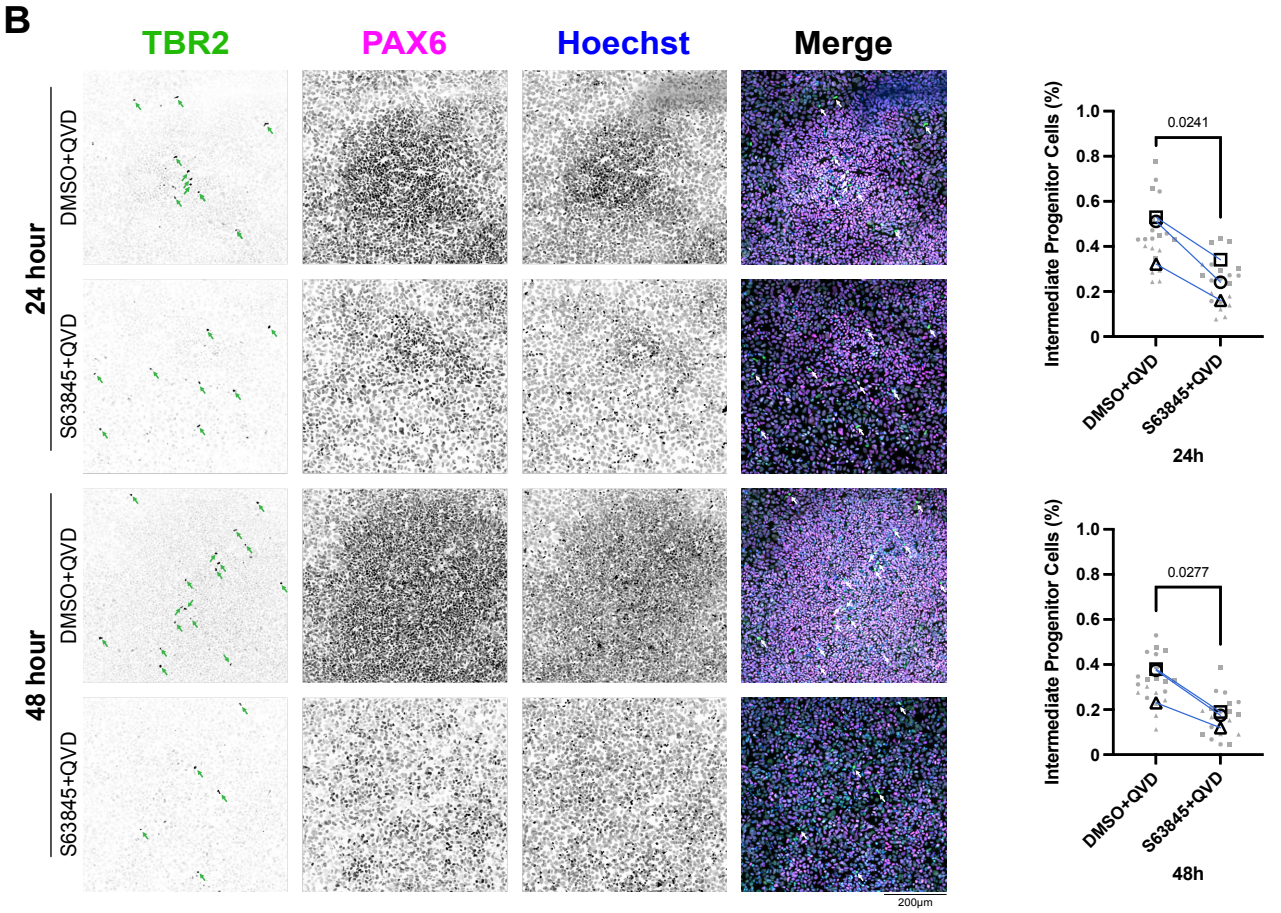
B
TBR2
PAX6
Hoechst
Merge
24 hour
DMSO+QVD
S63845+QVD
48 hour
DMSO+QVD
S63845+QVD
200µm
Intermediate Progenitor Cells (%)
0.0241
DMSO+QVD
S63845+QVD
24h
0.0277
48h

Figure 7

A

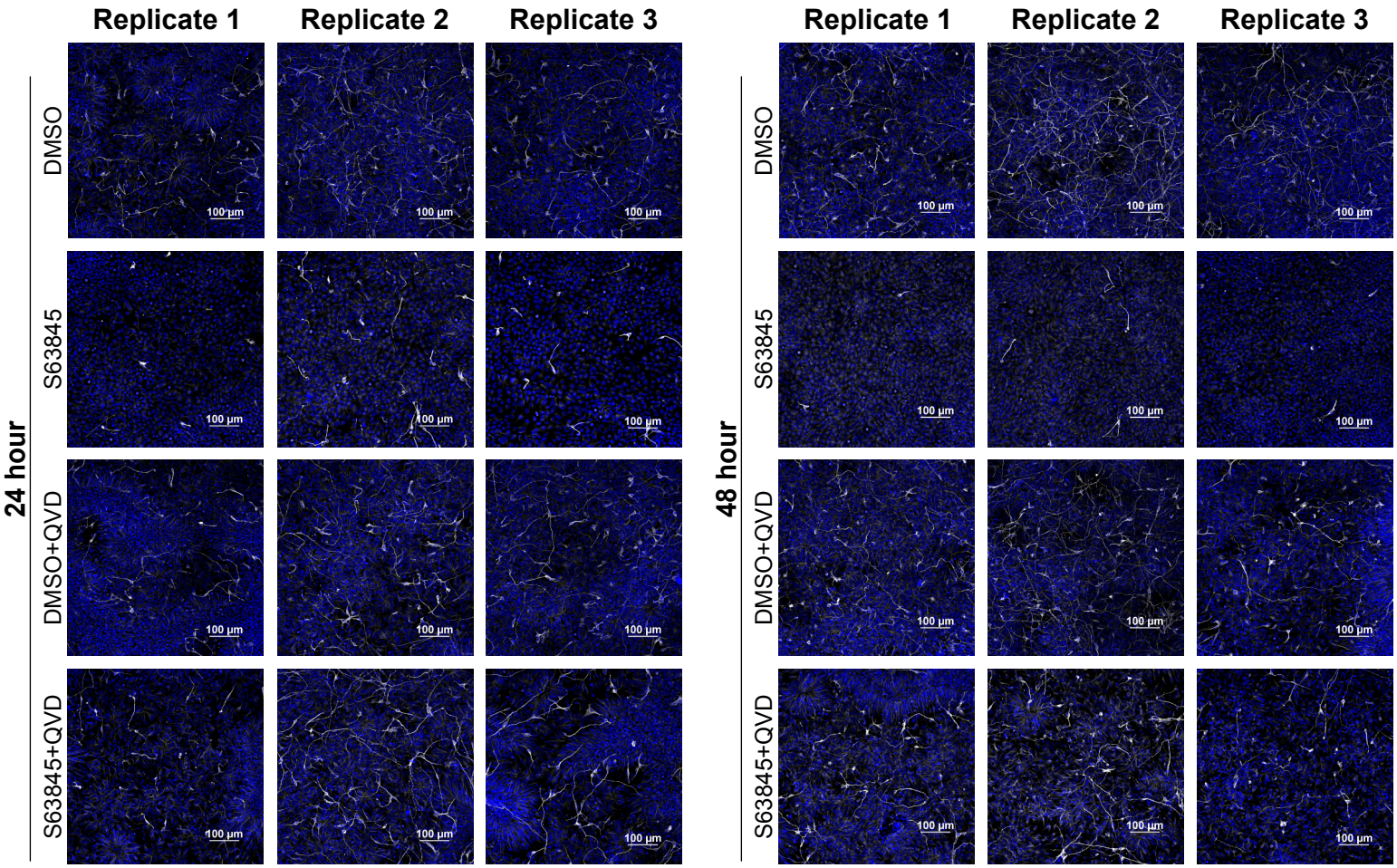
Replicate 1
Replicate 2
Replicate 3
24 hour
48 hour
DMSO
S63845
DMSO+QVD
S63845+QVD
100 µm